Low-carbon Economic Dispatch in Integrated Energy Systems: a Set-based Interval Optimization with Decision Support Under Uncertainties

Jiehui Zheng, *Member*, *IEEE*, Lexian Zhai, Mingming Tao, Wenhu Tang, *Senior Member*, *IEEE*, and Zhigang Li, *Senior Member*, *IEEE*

***Abstract*—The incorporation of high percentages of renewable resources into integrated energy systems (IES) is accelerating, and it becomes challenging to identify low-carbon economic dispatch options with significant uncertainties. This paper proposes an enhanced structure that combines hydrogen storage, power-to-gas, carbon capture and storage, and hydrogen fuel cells to extend CO_2 reduction pathways. The structure is embedded within an IES that considers multi-energy network constraints. First, the low-carbon economic dispatch model is formulated as a multi-objective interval optimization problem minimizing the total fuel cost and carbon emissions of the IES comprising electricity, heat, gas, and hydrogen subsystems. Then, the multi-objective optimization problem is solved by set-based group search interval optimizer (Set-GSIO) to construct an interval-based Pareto frontier while preserving the uncertainty information for decision-making. In addition, a decision support method based on Shannon entropy and the technique of ordering preferences for similarity of ideal solutions (TOPSIS) evaluates the interval solutions in terms of convergence, stability, and security. Finally, case studies are conducted on a modified IEEE30-bus system integrated with a 15-node gas network and a 32-node heat network to verify the effectiveness of the proposed architecture and approach. Furthermore, the proposed approach is demonstrated on a larger-scale test case, and simulation results verify its scalability.**

***Index Terms*—Integrated energy systems, low-carbon, uncertainty, interval optimization, decision-making.**

I. INTRODUCTION

In response to the escalating global climate crisis, China has committed to peaking its carbon emissions by 2030 and achieving carbon neutrality by 2060 [1]. The power generation sector, which is responsible for over 45% of national emissions [2], is central to this low-carbon transition. Consequently, large-scale integration of renewable energy sources (RES) has become a pivotal strategy for mitigating climate change. However, the inherent volatility and intermittency of RES, such as wind and solar power, pose significant challenges to grid stability and operational security, often leading to issues like energy curtailment [3]. This underscores the urgent need for advanced coordination of multi-energy resources to enhance system flexibility while reducing carbon emissions.

Integrated energy systems (IES), which couple electricity, heat, and natural gas networks, have emerged as a key enabling framework for the energy transition [4]. By synergistically operating diverse energy vectors, an IES can improve RES hosting capacity, boost overall energy efficiency, and increase operational flexibility [5]. However, while this deep integration of heterogeneous energy carriers offers clear advantageous, it also introduces notable operational complexities. Therefore, the principal challenge is shifted from managing a single energy vector to developing sophisticated dispatch strategies that can effectively coordinate diverse assets across multiple energy networks. The objective is to harness the full potential of multi-energy coupling to advance RES integration while ensuring the system operates economically and with low carbon emissions.

As a crucial interconnection between the electricity and natural gas systems, power-to-gas (P2G) couples electricity and gas networks by converting surplus renewable power into hydrogen via electrolysis (EL) and subsequently into synthetic natural gas (SNG) through methanation (MR) [6]–[8]. To further optimize the IES emission performance, several studies have explored the integration of P2G with other technologies. When combined with carbon capture and storage (CCS), P2G can reuse captured CO_2 to lower the carbon footprint

---

Received: March 1, 2025
Accepted: August 27, 2025

Jiehui Zheng, Lexian Zhai, Mingming Tao, and Wenhu Tang (corresponding author) are with the School of Electric Power Engineering, South China University of Technology, Guangzhou 510640, China (e-mail: zhengjh@scut.edu.cn; 202321015282@mail.scut.edu.cn; 202120115046@mail.scut.edu.cn; wenhutang@scut.edu.cn).

Zhigang Li is with the School of Science and Engineering, The Chinese University of Hong Kong (Shenzhen), Shenzhen 518172, China (e-mail: lizg@cuhk.edu.cn).

DOI: 10.23919/PCMP.2025.000183

[9], while hydrogen fuel cells (HFCs) further enhance system synergy and reduce carbon emissions [10]. A critical component for unlocking the full potential of P2G is the integration of hydrogen storage.

Dedicated hydrogen storage decouples the intermittent nature of RES from the operational demands of the IES, thereby improving the capacity for RES penetration and enhancing energy utilization efficiency [11]. The refined integration and optimization of the IES with hydrogen storage capabilities are critical for achieving substantial cost savings and reducing carbon emissions [12]. Reference [13] develops an electro-thermal coupling model for hydrogen storage units. Moreover, integrating hydrogen storage into an IES has demonstrated the potential to reduce carbon emissions by 43.8%, highlighting its effectiveness in advancing low-carbon energy solutions. Compared to existing systems, this approach not only enhances system flexibility but also reduces power input and marginal emissions by approximately 53% [14].

From a modeling perspective, the existing studies on IES optimization can be categorized into two distinct scales of analysis. The first approach operates at the component level and often considers the system as an energy hub or microgrid [10], [11], [15]. While these studies excel at optimizing internal energy conversion and management within localized boundaries, they typically simplify or neglect external network constraints. The second, which is a more comprehensive approach, operates at the network system level. This approach embeds the energy conversion units within the physical constraints of the wider electricity, gas, and thermal networks, explicitly modeling network topologies and multi-energy flow dynamics [16], [17]. While this network-aware modeling is more aligned with the realities of large-scale system dispatch, it introduces a significantly higher degree of modeling complexity and computational burden. Some relevant studies and their main contributions and associated technologies are summarized in Table I.

TABLE I
SUMMARY OF THE RELEVANT STUDIES ON THE OPTIMIZATION OF THE IES

Reference	Component type					Modeling perspective level		Objective	Uncertainty handling				Remarks
	P2G	CCS	CHP	ES	HFC	Component	Network		DO	SO	RO	IO	
[9]	√	√	√			√		Eco	√				Analyzes CHP, P2G, and CCS integration to reduce operating costs
[10]	√	√	√	√	√	√		Eco	√				Introduces an integrated component model for improved system synergy
[13]	√		√	√	√	√		Eco & Env	√				Develops electro-thermal coupling model for hydrogen storage
[15]	√	√		√		√		Eco & Env	√				An adaptive spiking neural P system enhances wind power utilization and reduces carbon emissions
[5]	√		√	√		√		Eco & Env		√			Proposes a hybrid natural gas pricing model with a tiered carbon trading system for low-carbon dispatch
[18]	√		√	√			√	Eco		√			Proposes a three-layer framework for regional IES planning with uncertainty management
[19]			√		√	√		Eco & Env			√		Develops a bi-level robust optimization framework for IES considering renewable-load uncertainty
[20]	√			√			√	Eco			√		Combining robust optimization enhances wind integration and reduces costs under renewable uncertainty
[21]	√	√	√	√		√		Eco				√	Proposes an interval multi-objective fuzzy optimization model for IES dual-phase scheduling
The method proposed in this paper	√	√	√	√	√		√	Eco & Env				√	Proposes a set-based interval low-carbon economic dispatch with decision support for network-constrained IES under uncertainty

Note: CHP represents combined heat and power; ES represents energy storage (including hydrogen or battery); Eco & Env represent economic and environmental objectives, respectively; DO represents deterministic optimization; SO represents stochastic optimization; RO represents robust optimization; IO represents interval optimization.

Beyond the structural and modeling complexities, a critical challenge in IES operational optimization is managing the inherent uncertainties, primarily stemming from the fluctuating nature of RES. A prevalent approach is stochastic optimization (SO), which models uncertainty through probability distributions, often generated from historical data via methods like Monte Carlo simulation [5], [18]. However, the efficacy of SO is contingent upon the availability of large-scale, high-fidelity datasets to construct probability density functions accurately, and the associated computational burden can be substantial. Also, it is often challenging for the decision-maker to obtain adequate data to accurately forecast or estimate the distributions of underlying uncertainty, limiting its practical applicability. To circumvent these data-intensive requirements, robust optimization (RO) has been widely adopted [19], [22]. RO ensures system reliability by optimizing against the worst-case realization of uncertainty within a predefined set. Nevertheless, the difficulty in adaptively tuning the level of conservatism to balance robustness and economic performance remains a significant drawback in RO [23]. Furthermore, at the network level, the high-dimensional and spatially distributed nature of uncertainty complicates the construction of an appropriate uncertainty set [24], potentially leading to the compounding of modeling errors. Additionally, the aforementioned frameworks often struggle to simultaneously optimize multiple objectives without a priori weight assignments or modified structure.

Compared to the aforementioned methods, interval optimization (IO), which characterizes uncertain variables using interval numbers defined only by their upper and lower bounds [25], offers a viable alternative. This representation alleviates the need for precise probability distributions, as boundary information is often more readily available than extensive historical data. By seeking to optimize the interval-valued objective function directly, IO can also yield less conservative outcomes than the worst-case approach of RO. Consequently, IO has been increasingly adopted for IES optimization under uncertainty [21], [26], [27]. However, applying IO to IES multi-objective dispatch introduces a unique challenge. While multi-attribute decision-making (MADM) methods like technique of ordering preferences for similarity of ideal solutions (TOPSIS) are commonly used to select a compromise solution from a Pareto-optimal set [28], [29], a critical issue arises when the objectives themselves become interval-valued due to uncertainty propagation. This propagation fundamentally complicates the solution process, as standard definitions of Pareto dominance and conventional MADM techniques are designed for crisp numerical values. Directly comparing and ranking interval outcomes to identify the optimal solution presents further difficulties in multi-objective optimization and decision-making models.

To address the aforementioned research gap, this paper develops a joint operational framework for P2G with CCS and HFC (PCH) units [10] by strategically integrating hydrogen storage. This integration refines the hydrogen flow process, significantly increasing the operational flexibility and energy utilization efficiency of the PCH unit. Compared to the component-level analyses [15], [19], [21], the enhanced PCH unit is embedded within a multi-energy network-constrained IES model. To address the dual challenges of RES uncertainty and interval-based multi-objective decision-making [21], [26], a set-based interval optimization framework combined with a decision support system is employed to determine the final dispatch solution. The main contributions of this paper are summarized as follows.

1) A combined low-carbon economic interval dispatch model for coupling electricity, heating, and gas networks considering uncertainties is established. A set-interval credibility strategy is developed to determine the interval values and map the uncertainty impact of decentralized buses directly onto the dispatch objectives.

2) The set-based group search interval optimizer (Set-GSIO) is developed to achieve the Pareto solutions of the formulated interval multi-objective optimization problem. The algorithm incorporates a set-driven evolutionary strategy, whereby the interval problem transformation and a dual-producer mechanism guide the search process.

3) A decision-making support method based on the Shannon entropy and TOPSIS method to handle the interval-valued Pareto front pragmatically is proposed. The effectiveness of the solution framework is validated using the generated sampling scenarios and a sensitivity analysis on the uncertainty forecast error.

The remaining sections of this paper are organized as follows. Section II introduces the IES coupling hydrogen storage with the modified PCH structure. Section III presents the mathematical modeling for the low-carbon economic dispatch of the IES. The details of the Set-GSIO interval optimization algorithm and the decision-making approach are presented in Section IV. Case studies are discussed to evaluate the effectiveness of the proposed structure and approach in Section V. Finally, the conclusion and future work are presented in Section VI.

II. IES MODELING

Figure 1 depicts a schematic overview of the low-carbon dispatch model for the IES, which consists of coupled electricity, heating, and gas networks. The combined heat and power (CHP) units produce both electricity and heat, while the CCS captures CO_2 from exhaust gases for potential use in methanation. Furthermore, the hydrogen subsystem is composed of multiple components, including the EL, HFC, and hydrogen storage unit. The green color highlights the hydrogen flow, representing the dynamic integration of hydrogen as an energy carrier into the gas and electricity subsystems.

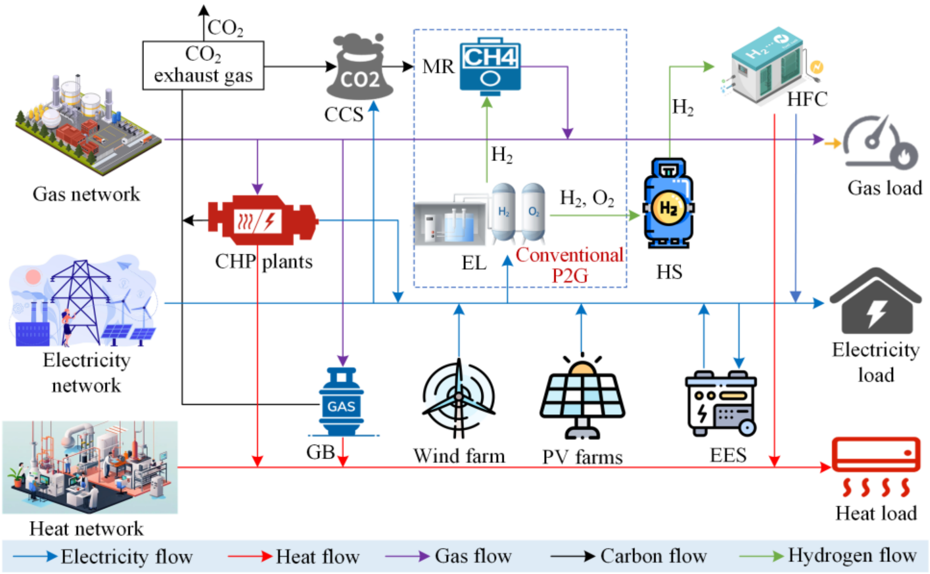

Fig. 1. The IES structure block diagram.

A. PCH Structure Combined with Hydrogen Storage

The structure integrating P2G with both CCS and HFC is denoted as the PCH structure [10] which enhances hydrogen utilization. However, considering hydrogen storage as a vital pathway for promoting RES penetration, combining hydrogen storage equipment with the PCH structure significantly enhances hydrogen utilization and the flexibility of the PCH structure.

1) P2G Equipment Model

A proton exchange membrane water electrolyzer (PEMWE) model is employed for EL due to its rapid startup and high efficiency potential [21], which is mathematically defined as:

$$E_{\mathrm{EL,H_2},t}=\eta_{\mathrm{EL}}P_{\mathrm{EL},t} \tag{1}$$

where $E_{\mathrm{EL,H_2},t}$ is the hydrogen power produced by the EL unit; $P_{\mathrm{EL},t}$ represents the electricity consumed; and η_{EL} is the energy conversion efficiency coefficient of EL.

H_2 and CO_2 are synthesized into synthetic natural gas (SNG) in the MR, which can be formulated as [10]:

$$\begin{cases} P_{\mathrm{MR,g},t}=\eta_{\mathrm{MR}}E_{\mathrm{MR,H_2},t} \\ C_{\mathrm{CO_2},t}=\varpi P_{\mathrm{MR,g},t} \end{cases} \tag{2}$$

where $E_{\mathrm{MR,H_2},t}$ and $P_{\mathrm{MR,g},t}$ are the hydrogen power consumed and the SNG power produced by the MR, respectively; $C_{\mathrm{CO_2},t}$ represents the carbon sequestration capacity of the MR; while η_{MR} and ϖ represent the energy and carbon gas conversion efficiency of the MR, respectively.

2) CCS Equipment Model

The combined CCS and genset operation system can be utilized as a stabilized carbon source for the P2G, as demonstrated by the following formula [10]:

$$P_{\mathrm{CCS},t}=\chi C_{\mathrm{CC},t} \tag{3}$$

where $P_{\mathrm{CCS},t}$ represents the operation power of the CCS; $C_{\mathrm{CC},t}$ is the CO_2 absorption rate of CCS; and χ is the corresponding absorption coefficient.

3) HFC Equipment Model

The solid oxide fuel cell (SOFC) mathematical model is formulated as follows [10]:

$$\begin{cases} P_{\mathrm{HFC,e},t}=\eta_{\mathrm{HFC,e}}P_{\mathrm{HFC},t} \\ Q_{\mathrm{HFC,h},t}=\eta_{\mathrm{HFC,h}}P_{\mathrm{HFC},t} \end{cases} \tag{4}$$

where $P_{\mathrm{HFC,e},t}$ and $Q_{\mathrm{HFC,h},t}$ represent the electrical and thermal output power from the HFC, respectively; $P_{\mathrm{HFC},t}$ is the input power to HFC; while $\eta_{\mathrm{HFC,e}}$ and $\eta_{\mathrm{HFC,h}}$ represent the conversion efficiency of the HFC to the electrical and thermal power, respectively.

B. Analysis Approach for PCH and Hydrogen Storage

It is crucial to emphasize that the PCH structure's operational status is influenced by both the EL and the hydrogen storage unit. This determination is guided by the hydrogen balance constraint, which is shown in (5). The hydrogen storage unit can adjust the total hydrogen inventory during the entire operational process.

$$E_{\mathrm{EL,H_2},t}=E_{\mathrm{HFC,H_2},t}+E_{\mathrm{MR,H_2},t}-E_{\mathrm{HS,H_2},t} \tag{5}$$

where $E_{\mathrm{HFC,H_2},t}$ and $E_{\mathrm{MR,H_2},t}$ represent the hydrogen consumed by the HFC and MR; while $E_{\mathrm{HS,H_2},t}$ is the hydrogen output of the hydrogen storage unit.

The hydrogen storage unit and the EL influence the total hydrogen in this mode consumption by the MR and HFC units at a given moment. The MR unit is responsible for the reduction of CO_2 by converting hydrogen into synthesis gas, which serves as fuel for the CHP unit. The HFC combusts hydrogen, releasing both thermal and electrical energy. Once the operational states of the EL or hydrogen storage unit are known, a strategic interaction arises between the MR and HFC units. In other words, the operational state of one unit will be a determining factor in the state of the other. Consequently, an analysis of the thermal, electrical, and gas operational characteristics of PCH structure is conducted using two distinct energy coupling methods. The mathematical models are respectively represented by (6)–(8) and (9)–(11) [10].

$$P_{\mathrm{PCH\_SGWH}} = (1+\chi\varpi\eta_{\mathrm{MR}}\eta_{\mathrm{EL}})(P_{\mathrm{EL},t}+E_{\mathrm{HS,H_2},t}) - (\chi\varpi\eta_{\mathrm{MR}}+\eta_{\mathrm{HFC,e}})P_{\mathrm{HFC},t} \tag{6}$$

$$P_{\mathrm{MR,g},t} = \frac{\eta_{\mathrm{EL}}\eta_{\mathrm{MR}}}{1+\chi\varpi\eta_{\mathrm{MR}}\eta_{\mathrm{EL}}}P_{\mathrm{PCH\_SGWH}} - \frac{\eta_{\mathrm{MR}}(1-\eta_{\mathrm{EL}}\eta_{\mathrm{HFC,e}})}{1+\chi\varpi\eta_{\mathrm{MR}}\eta_{\mathrm{EL}}}P_{\mathrm{HFC},t} \tag{7}$$

$$Q_{\mathrm{HFC,h},t} = \eta_{\mathrm{HFC,h}}P_{\mathrm{HFC},t} \tag{8}$$

where $P_{\mathrm{PCH\_SGWH}}$ represents the required electricity in this mode; and $P_{\mathrm{MR,g},t}$ is the generated natural gas. In this mode, HFC serves as the determining factor, and the operational state of HFC will determine the states of MR and CCS.

$$P_{\mathrm{c\_en}} = (1-\eta_{\mathrm{HFC,e}}\eta_{\mathrm{EL}})(P_{\mathrm{EL},t}+E_{\mathrm{HS,H_2},t}) + \left(\chi+\frac{\eta_{\mathrm{HFC,e}}}{\varpi\eta_{\mathrm{MR}}}\right)E_{\mathrm{MR,H_2},t} \tag{9}$$

$$Q_{\mathrm{HFC,h},t} = \frac{\eta_{\mathrm{HFC,h}}\eta_{\mathrm{EL}}}{1-\eta_{\mathrm{HFC,e}}\eta_{\mathrm{EL}}}P_{\mathrm{c\_en}} - \frac{\eta_{\mathrm{HFC,h}}(\eta_{\mathrm{EL}}\eta_{\mathrm{MR}}\chi\varpi+1)}{\eta_{\mathrm{MR}}(1-\eta_{\mathrm{HFC,e}}\eta_{\mathrm{EL}})}P_{\mathrm{MR,g},t} \tag{10}$$

$$P_{\mathrm{MR,g},t} = E_{\mathrm{MR,H_2},t}\eta_{\mathrm{MR}} \tag{11}$$

where $P_{\mathrm{c\_en}}$ represents the required electricity in this scenario. And CCS is the primary determinant of the operational state of MR and HFC.

C. CHP Unit Model

The CHP unit model can be formulated as follows [21]:

$$P_{\mathrm{CHP,e},t} = \frac{V_{\mathrm{gt},t}\eta_{\mathrm{gt,e}}L_{\mathrm{LHV,ng}}}{\Delta t} \tag{12}$$

$$Q_{\mathrm{CHP,h},t} = \alpha_{\mathrm{chp}}P_{\mathrm{CHP,e},t} \tag{13}$$

where $P_{\mathrm{CHP,e},t}$ and $Q_{\mathrm{CHP,h},t}$ are the output electrical and thermal power of the CHP unit; $V_{\mathrm{gt},t}$ and $\eta_{\mathrm{gt,e}}$ are the gas consumption and the efficiency of the CHP unit, respectively; $L_{\mathrm{LHV,ng}}$ is the low calorific value of natural gas; and α_{chp} is the thermal-electricity ratio of the CHP unit.

D. Compressor Model

The mathematical model for the compressor i between nodes m and n is expressed as follows [16]:

$$f_{mn}^{\mathrm{CMP}} = \frac{H_{\mathrm{CMP},k}}{B_k\left[\left(\dfrac{\pi_n}{\pi_m}\right)^{Z_k\times\left(\frac{\alpha-1}{\alpha}\right)}-1\right]} \tag{14}$$

$$P_{\mathrm{CMP},k} = \eta_{\mathrm{CMP},k}H_{\mathrm{CMP},k} \tag{15}$$

where $H_{\mathrm{CMP},k}$ signifies the horsepower consumption of the kth compressor; Z_k represents the gas compression factor at the compressor inlet; T_k is the suction temperature; α stands for the specific heat ratio and B_k is a parameter related to compressor suction temperature and efficiency; while $P_{\mathrm{CMP},k}$ and $\eta_{\mathrm{CMP},k}$ represent the power and the coefficient of relationship between power and horsepower for a specific compressor k, respectively.

E. Gas Boiler Model

The gas boiler (GB) unit is mathematically expressed as [10]:

$$Q_{\mathrm{GB,h},t} = \eta_{\mathrm{GB,h}}P_{\mathrm{GB,g},t} \tag{16}$$

where $Q_{\mathrm{GB,h},t}$ and $P_{\mathrm{GB,g},t}$ represent the thermal and gas consumption power of GB device, respectively; and $\eta_{\mathrm{GB,h}}$ is the conversion efficiency of the GB.

III. LOW-CARBON ECONOMIC DISPATCH MODEL OF IES

A. Objective Function and Decision-making Metrics

This paper considers the two objective functions of the overall operation of the IES: total fuel cost (TFC) and carbon emissions (CE). In addition, power loss (PL), sum voltage deviations (SVD), and node sum pressure deviations (SPD) are considered as decision-making metrics to ensure safe operation.

1) Total Fuel Costs

TFC encompasses the fuel expenses of the thermal power units and natural gas supply charges, which can be expressed as follows [30]:

$$F_{\mathrm{TFC}} = \sum_{t=1}^{T}\left(F_{\mathrm{G_u}}(P_{\mathrm{G}_u^t}) + C_{\mathrm{g}}Q_{\mathrm{g},t}^{\mathrm{g}}\right) \tag{17}$$

$$F_{\mathrm{G}_u}(P_{\mathrm{G}_u^t}) = \sum_{u=1}^{N_{\mathrm{G}}}\left(a_u\left(P_{\mathrm{G}_u^t}\right)^2 + b_uP_{\mathrm{G}_u^t} + c_u\right) \tag{18}$$

where F_{TFC} is the total cost over the entire time horizon; $F_{\mathrm{G}_u}(P_{\mathrm{G}_u^t})$ is the fuel costs of generator u; a_u, b_u and c_u are the corresponding coefficients of generator u; $P_{\mathrm{G}_u^t}$ is the active power output of generator u; C_{g} is the unit cost of natural gas; and $Q_{\mathrm{g},t}^{\mathrm{g}}$ represents the gas purchase quantity.

2) Carbon Emissions

The carbon emissions calculation considers the $\mathrm{CO_2}$ absorbed by the thermal, CHP, and CCS units, and is given as:

$$\begin{aligned} F_{\mathrm{CE}} = {} & \sum_{t=1}^{T}\left(F_{\mathrm{C}_u}(P_{\mathrm{G}_u^t})\right)+\sum_{t=1}^{T}\Big(\alpha_2(P_{\mathrm{CHP,e},t}+P_{\mathrm{GB,g},t})^2 + \\ & \beta_2(P_{\mathrm{CHP,e},t}+P_{\mathrm{GB,g},t})+\gamma_2\Big)-\sum_{t=1}^{T}C_{\mathrm{CO_2},t} \end{aligned} \tag{19}$$

$$F_{\mathrm{C}_u}(P_{\mathrm{G}_u^t})=\sum_{i=1}^{N_{\mathrm{G}}}\left(\alpha_1\left(P_{\mathrm{G}_u^t}\right)^2+\beta_1 P_{\mathrm{G}_u^t}+\gamma_1\right) \tag{20}$$

where F_{CE} represents the total CE of the IES; $F_{\mathrm{C}_u}(P_{\mathrm{G}_u^t})$ is the CE of generator u; $C_{\mathrm{CO_2},t}$ is the amount of $\mathrm{CO_2}$ absorbed by CCS during time *t*; while α_1, α_2, β_1, β_2, γ_1, and γ_2 are the emission coefficients.

3) Decision-making Metrics

The PL, SVD, and SPD, used as the decision-making metrics can be formulated as follows [30]:

$$F_{\mathrm{PL}}(t)=\sum_{l=1}^{N_{\mathrm{branch}}} g_l\left[V_i^2-V_j^2-2V_iV_j\cos(\theta_i-\theta_j)\right] \tag{21}$$

$$F_{\mathrm{SVD}}(t)=\sum_{i=1}^{N_{\mathrm{node}}}\left|V_i-V_{\mathrm{ref}}\right| \tag{22}$$

$$F_{\mathrm{SPD}}(t)=\sum_{g=1}^{N_{\mathrm{gnode}}}\left|p_x-p_{\mathrm{ref}}\right| \tag{23}$$

where g_l is the conductance of a transmission line l connected between the *i*th and *j*th bus; while V_i, V_j, θ_i, θ_j are the voltage magnitudes and phase angles of the *i*th and *j*th buses; V_{ref} and p_{ref} are the reference voltage and pressure, respectively.

B. Constraints

A set of constraints that ensures the physical feasibility of the dispatch solution can be categorized into component-level and network-level constraints of the IES.

1) Component-level Constraints

The component-level constraints include the conventional operation and capacity limits of CHP, HFC, EL, MR, CCS, GB, battery, and hydrogen energy storage, which are detailed in Appendix A.

2) Network-level Constraints

To accurately capture the intricate relationships within the different subsystems of the IES, the physical laws that govern the electricity, natural gas, and heating networks are explicitly modeled.

a) Power Balance

The AC power flow equations are enforced to maintain the power balance at each bus in the electricity network. In a compact matrix form, these constraints are expressed as:

$$\boldsymbol{F}_{\mathrm{e}}(\boldsymbol{X}_{\mathrm{e}})=\begin{bmatrix}\Delta\boldsymbol{P}_{\mathrm{S}}\\ \Delta\boldsymbol{Q}_{\mathrm{S}}\end{bmatrix}=\begin{bmatrix}\mathrm{Real}\left(\boldsymbol{V}(\boldsymbol{YV})^*\right)-\boldsymbol{P}_{\mathrm{S}}\\ \mathrm{Imag}\left(\boldsymbol{V}(\boldsymbol{YV})^*\right)-\boldsymbol{Q}_{\mathrm{S}}\end{bmatrix}=\boldsymbol{0} \tag{24}$$

where $\boldsymbol{P}_{\mathrm{S}}$ and $\boldsymbol{Q}_{\mathrm{S}}$ are the vectors of active and reactive power injections at each node; $\boldsymbol{Y}$ is the nodal admittance matrix; $\boldsymbol{V}$ is the vector of bus voltages; $\mathrm{Real}(\cdot)$ and $\mathrm{Imag}(\cdot)$ are operators that extract the real and imaginary parts, respectively; and the state vector $\boldsymbol{X}_{\mathrm{e}}$ comprises the bus voltage angles and magnitudes. Additional constraints include limits on branch power flows and bus voltage magnitudes.

b) Natural Gas Network Constraints

The steady-state operation of the gas network is described by a set of nonlinear equations representing nodal flow balance and the physics of pipelines and compressors. These constraints can be expressed in a unified matrix form $\boldsymbol{F}_{\mathrm{g}}(\boldsymbol{X}_{\mathrm{g}})=\boldsymbol{0}$ as follows [16]:

$$\boldsymbol{F}_{\mathrm{g}}(\boldsymbol{X}_{\mathrm{g}})=\begin{bmatrix}\Delta\boldsymbol{f}_{\mathrm{gas}}\\ \Delta\boldsymbol{d}\end{bmatrix}=\begin{bmatrix}\boldsymbol{A}_{\mathrm{g}}\boldsymbol{f}^{\mathrm{pipe}}+\boldsymbol{U}_{\mathrm{g}}\boldsymbol{f}^{\mathrm{comp}}-\boldsymbol{f}_{\mathrm{gas}}\\ \boldsymbol{W}_1\boldsymbol{\pi}_{\mathrm{s}}^2+\boldsymbol{W}_2\boldsymbol{\pi}_{\mathrm{e}}^2+\boldsymbol{W}_3\boldsymbol{f}^{\mathrm{comp}}-\boldsymbol{d}\end{bmatrix} \tag{25}$$

where $\boldsymbol{A}_{\mathrm{g}}$ and $\boldsymbol{U}_{\mathrm{g}}$ are the node-to-pipeline and node to compressor incidence matrices, respectively; the vectors $\boldsymbol{f}^{\mathrm{pipe}}$, $\boldsymbol{f}^{\mathrm{comp}}$, and $\boldsymbol{f}_{\mathrm{gas}}$ represent gas flows in pipelines, compressors, and at nodal injection points; the state vector $\boldsymbol{X}_{\mathrm{g}}$ includes nodal pressures and compressor flow rates; $\boldsymbol{W}_1$, $\boldsymbol{W}_2$, and $\boldsymbol{W}_3$ are the coefficient matrix, which are driven from the compressor energy consumption equation; $\boldsymbol{\pi}_{\mathrm{s}}$ and $\boldsymbol{\pi}_{\mathrm{e}}$ are the gas pressures at its start and end nodes; while $\Delta\boldsymbol{d}=\boldsymbol{0}$ models the operational constraints of the compressors. The pipeline flow $\boldsymbol{f}_p^{\mathrm{pipe}}$ is characterized by the Weymouth equation:

$$\boldsymbol{f}_p^{\mathrm{pipe}}=C_p\times\mathrm{sign}(\pi_{\mathrm{s}}-\pi_{\mathrm{e}})\sqrt{|\pi_{\mathrm{s}}^2-\pi_{\mathrm{e}}^2|} \tag{26}$$

where C_p is the Weymouth constant for pipeline p.

c) Heating Network Constraints

The thermal-hydraulic behavior of the district heating network is governed by the principles of mass and energy conservation. The unified energy flow constraints, denoted as $\boldsymbol{F}_{\mathrm{h}}(\boldsymbol{X}_{\mathrm{h}})=\boldsymbol{0}$, consist of the nodal energy balance equations for both the supply and return networks [16]. For the supply network, the balance equation is formulated as:

$$(\boldsymbol{A}_{\mathrm{h},2}\boldsymbol{m})\odot\boldsymbol{T}_{\mathrm{sn}}-\boldsymbol{A}_{\mathrm{h},2}\left[(\boldsymbol{B}_{\mathrm{h},1}\boldsymbol{T}_{\mathrm{sn}})\odot\boldsymbol{\Psi}\right]=\boldsymbol{0} \tag{27}$$

$$\boldsymbol{\Psi}=\boldsymbol{m}\odot\exp\left(-\frac{\lambda L}{H_{\mathrm{p}}\boldsymbol{m}}\right) \tag{28}$$

where the state vector $\boldsymbol{X}_{\mathrm{h}}$ comprises nodal temperatures and mass flow rates; while physical constants λ, L, and H_{p} represent the heat transfer coefficient, pipe length, and water's specific heat capacity, respectively; the vectors $\boldsymbol{m}$ is the mass flow rates of pipe; the auxiliary vector $\boldsymbol{\Psi}$ is introduced to represent the heat preservation factor for each pipe during transportation.

For the return network, the energy balance accounts for heat extraction at load nodes:

$$(\boldsymbol{A}_{\mathrm{h},1}\boldsymbol{m}+\boldsymbol{m}_{\mathrm{q}})\odot\boldsymbol{T}_{\mathrm{rn}}-\boldsymbol{A}_{\mathrm{h},1}\left[(\boldsymbol{B}_{\mathrm{h},2}\boldsymbol{T}_{\mathrm{rn}})\odot\boldsymbol{\Psi}\right]-\boldsymbol{m}_{\mathrm{q}}\odot\boldsymbol{T}_{\mathrm{o}}=\boldsymbol{0} \tag{29}$$

where $\boldsymbol{A}_{\mathrm{h},1}/\boldsymbol{A}_{\mathrm{h},2}$ and $\boldsymbol{A}_{\mathrm{h},2}/\boldsymbol{B}_{\mathrm{h},2}$ are the association matrices for the return/supply networks; while $\boldsymbol{T}_{\mathrm{sn}}$ and $\boldsymbol{T}_{\mathrm{rn}}$ represent the nodal temperatures in the supply and return pipes, respectively; furthermore, $\boldsymbol{m}_{\mathrm{q}}$ is the load mass flow; and $\boldsymbol{T}_{\mathrm{o}}$ is the temperature of water returning from the loads.

IV. SOLUTION METHODS

The proposed solution methodology, illustrated in Fig. 2, presents a hierarchical framework for solving the formulated interval low-carbon economic dispatch problem. The framework utilizes the Set-GSIO algorithm to explore the solution space and approximate the interval Pareto front. A critical step within the fitness evaluation of the Set-GSIO is the multi-energy flow calculation. To efficiently solve the coupled network equations and verify the physical constraints of each candidate dispatch solution, a gradient descent-based iterative method is adopted [16]. Finally, once the set of non-dominated solutions is obtained, an MADM module employing the Shannon entropy-based TOPSIS method is used to systematically rank the interval outcomes and identify the optimal compromise solution.

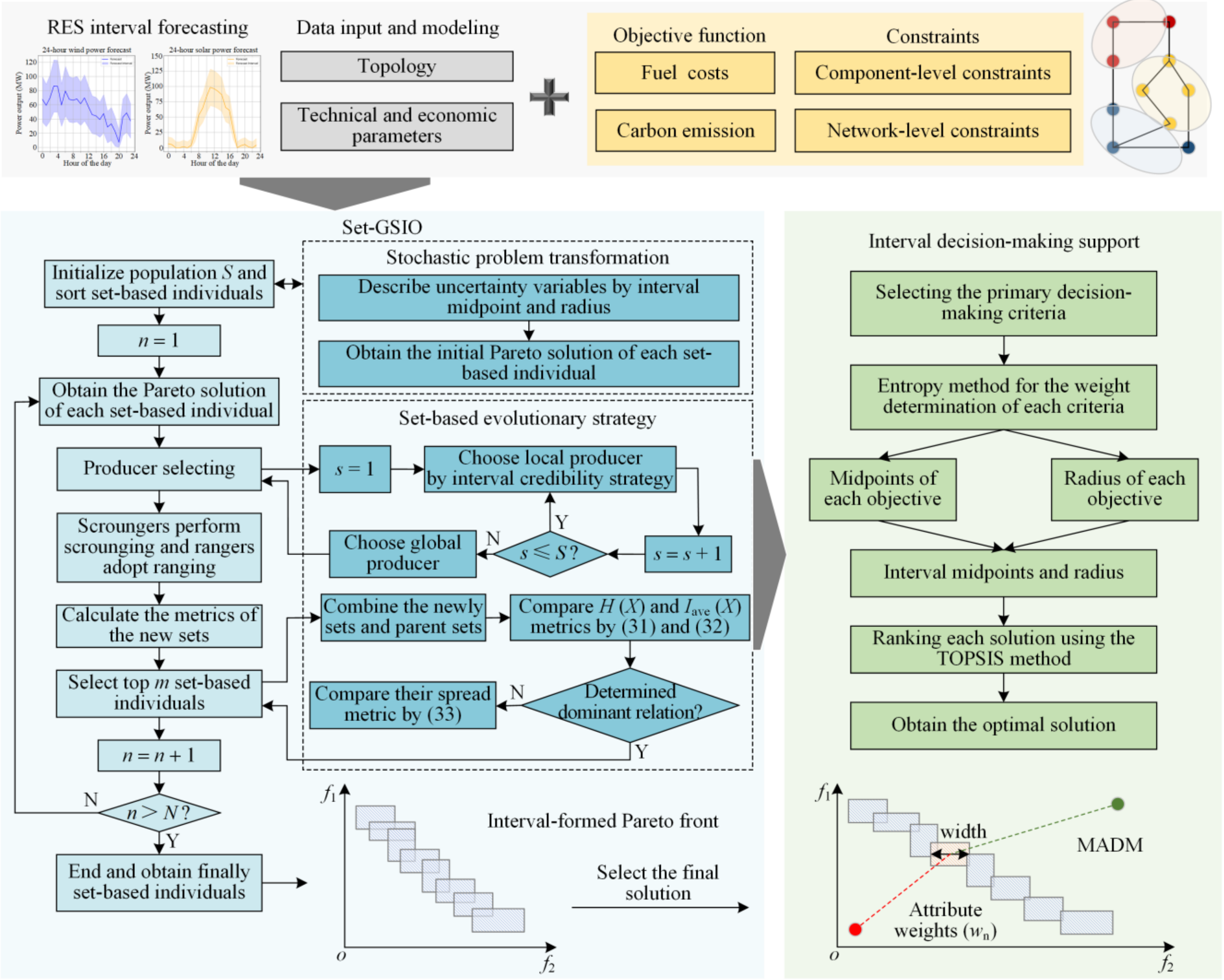

Fig. 2. Interval optimization and decision-making framework for low-carbon IES dispatch.

A. Uncertainty Description and Set-interval Domination

In this paper, the model describes objective functions under uncertainty through intervals $\left[\underline{f}(\boldsymbol{x}_{\mathrm{d}},\boldsymbol{u}_{\mathrm{d}}),\overline{f}(\boldsymbol{x}_{\mathrm{d}},\boldsymbol{u}_{\mathrm{d}})\right]$, which are determined by the following formulas:

$$\begin{cases}\underline{f}(\boldsymbol{x}_{\mathrm{d}},\boldsymbol{u}_{\mathrm{d}})=\min_{\boldsymbol{u}_{\mathrm{d}}} f(\boldsymbol{x}_{\mathrm{d}},\boldsymbol{u}_{\mathrm{d}})\\ \overline{f}(\boldsymbol{x}_{\mathrm{d}},\boldsymbol{u}_{\mathrm{d}})=\max_{\boldsymbol{u}_{\mathrm{d}}} f(\boldsymbol{x}_{\mathrm{d}},\boldsymbol{u}_{\mathrm{d}})\end{cases} \tag{30}$$

where $\boldsymbol{x}_{\mathrm{d}}$ is the set of decision variables, including the active power output of each generator $P_{\mathrm{G}_u^t}$, the hydrogen power consumed by MR $P_{\mathrm{MR},t}$, the input power of HFC $P_{\mathrm{HFC},t}$, the hydrogen output of the hydrogen storage unit $P_{\mathrm{HS,H_2},t}$, the gas consumption power of GB $P_{\mathrm{GB,g},t}$, and the output power of the battery energy storage system $P_{\mathrm{ES,e},t}$; $\boldsymbol{u}$ represents a collection of stochastic variables, corresponding to the uncertain outputs from wind turbines (WTs) and photovoltaic (PV). To characterize these uncertainty variables, an interval method is employed, as:

$$\boldsymbol{u}_{\mathrm{d}}^{\mathrm{T}}=\left[P_{\mathrm{WG}_1},\cdots,P_{\mathrm{WG}_{N_{\mathrm{WT}}}},P_{\mathrm{PV}_1},\cdots,P_{\mathrm{PV}_{N_{\mathrm{PV}}}}\right] \tag{31}$$

where variables $P_{\mathrm{WG},t}$, and $P_{\mathrm{PV},t}$ represent the lower and upper bounds of the uncertain power outputs, respectively; N_{WT} and N_{PV} represent the number of the WT and PV units.

The representation of objectives as intervals necessitates a mechanism to select the producers with the optimal values for each goal, especially when intervals overlap. To address this, the set-interval credibility strategy is developed that establishes a dominance relationship between any two interval-valued solutions, $A_{\mathrm{int}}=\left[\underline{a_{\mathrm{int}}},\overline{a_{\mathrm{int}}}\right]$ and $B_{\mathrm{int}}=\left[\underline{b_{\mathrm{int}}},\overline{b_{\mathrm{int}}}\right]$. This strategy quantifies the degree to which one interval solution is superior to another by calculating the set-interval credibility $P_{\mathrm{cre}}(A_{\mathrm{int}}<B_{\mathrm{int}})$, as:

$$\begin{cases} P_{\mathrm{cre}}(A_{\mathrm{int}}<B_{\mathrm{int}})=\dfrac{\mathrm{Dis}(B_{\mathrm{int}},D)}{\mathrm{Dis}(A_{\mathrm{int}},D)+\mathrm{Dis}(B_{\mathrm{int}},D)} \\ \mathrm{Dis}(A_{\mathrm{int}},D)=\max\left\{\left|\underline{a_{\mathrm{int}}}-D_{\mathrm{L}}\right|,\left|\overline{a_{\mathrm{int}}}-D_{\mathrm{R}}\right|\right\} \\ \mathrm{Dis}(B_{\mathrm{int}},D)=\max\left\{\left|\underline{b_{\mathrm{int}}}-D_{\mathrm{L}}\right|,\left|\overline{b_{\mathrm{int}}}-D_{\mathrm{R}}\right|\right\} \\ D_{\mathrm{L}}=\min\left\{\underline{a_{\mathrm{int}}},\underline{b_{\mathrm{int}}}\right\} \\ D_{\mathrm{R}}=\min\left\{\left\{\underline{a_{\mathrm{int}}},\underline{b_{\mathrm{int}}},\overline{a_{\mathrm{int}}},\overline{b_{\mathrm{int}}}\right\}\setminus\left\{D_{\mathrm{L}}\right\}\right\} \end{cases} \tag{32}$$

Based on this credibility, if $P_{\mathrm{rel}}(A_{\mathrm{int}}<B_{\mathrm{int}})>0.5$, then A_{int} is considered a better producer than B_{int}. This defines the positive degree of the interval objective values using only the upper and lower boundary output information of the renewables.

B. Problem Transformation

The objective of this subsection is to reformulate the problem containing uncertainty into a deterministic bi-objective problem, which is achieved by leveraging the interval hypervolume (HV) and average inaccuracy metrics. The HV metric captures the distribution of representative points along the Pareto front and assesses the convergence efficiency of the true Pareto front under the most adverse conditions. In contrast, the average inaccuracy metric quantifies the variability of Pareto optimal solutions attributable to stochastic variables. The formal definitions of the interval HV metric and the average inaccuracy are given as:

$$\begin{gathered} H(\boldsymbol{X}_{\mathrm{P}})=\left[\underline{H(\boldsymbol{X}_{\mathrm{P}})},\overline{H(\boldsymbol{X}_{\mathrm{P}})}\right]= \\ \wedge\left(\bigcup_{\boldsymbol{x}_{\mathrm{P}}\in\boldsymbol{X}_{\mathrm{P}}}\left\{\boldsymbol{y}\in\mathbb{R}\mid\boldsymbol{x}_{\mathrm{ref}}\prec\boldsymbol{y}\prec\boldsymbol{x}_{\mathrm{P}}\right\}\right) \end{gathered} \tag{33}$$

$$I_{\mathrm{ave}}(\boldsymbol{X}_{\mathrm{P}})=\frac{\sum\limits_{\boldsymbol{x}_{\mathrm{P}}\in\boldsymbol{X}_{\mathrm{P}}}\sum\limits_{m=1}^{M}\left(\overline{f}\left(\boldsymbol{x}_{\mathrm{P}},\boldsymbol{c}_m\right)-\underline{f}\left(\boldsymbol{x}_{\mathrm{P}},\boldsymbol{c}_m\right)\right)}{X_{\mathrm{num}}} \tag{34}$$

where $\boldsymbol{X}_{\mathrm{P}}$ is an approximate Pareto-optimal solution set; $\boldsymbol{x}_{\mathrm{P}}$ is a solution in $\boldsymbol{X}_{\mathrm{P}}$; $\boldsymbol{y}\in\mathbb{R}$ serves as an auxiliary vector in the objective space for volume integration; $\overline{H(\boldsymbol{X}_{\mathrm{P}})}$ and $\underline{H(\boldsymbol{X}_{\mathrm{P}})}$ represent the best-case and the worst-case HV, respectively; $\boldsymbol{x}_{\mathrm{ref}}$ is the reference point; $\wedge$ is the Lebesgue measure; $\boldsymbol{c}_m$ represents the vector of uncertainty parameters associated with the mth objective function; and X_{num} is the size of Pareto-optimal solution.

Therefore, during the evolutionary process, a superior set is identified by comparing two set-based metrics. In cases where one metric is superior and the other is inferior, a spread metric is employed to determine the preference:

$$S_{\mathrm{Spread}}(\boldsymbol{X}_{\mathrm{P}})=\sqrt{\sum_{m=1}^{M}\left(\max\overline{f}(\boldsymbol{x}_{\mathrm{P}},\boldsymbol{c}_m)-\min\underline{f}(\boldsymbol{x}_{\mathrm{P}},\boldsymbol{c}_m)\right)^2} \tag{35}$$

The larger the $S_{\mathrm{Spread}}(\boldsymbol{X}_{\mathrm{P}})$, the broaden the distribution of its corresponding front.

C. Set-GSIO Algorithm

In this paper, the proposed Set-GSIO algorithm is employed to solve the interval optimization model. The algorithm leverages set-based bi-objective transformations as introduced in Section IV.B and evolutionary roles with producers, scroungers, and rangers [31] to refine the interval Pareto archives iteratively. In this framework, evolutionary searches are driven by scroungers that update their positions by simultaneously learning from local and global producers, as well as from archived Pareto-optimal solutions. Rangers are responsible for random exploration. Figure 3 provides a visual representation of the evolutionary strategy of Set-GSIO. This process involves evaluating and selecting entire parent and offspring subpopulations to advance to the next generation via a set-driven process. The pseudocode for the Set-GSIO algorithm is presented in Algorithm 1.

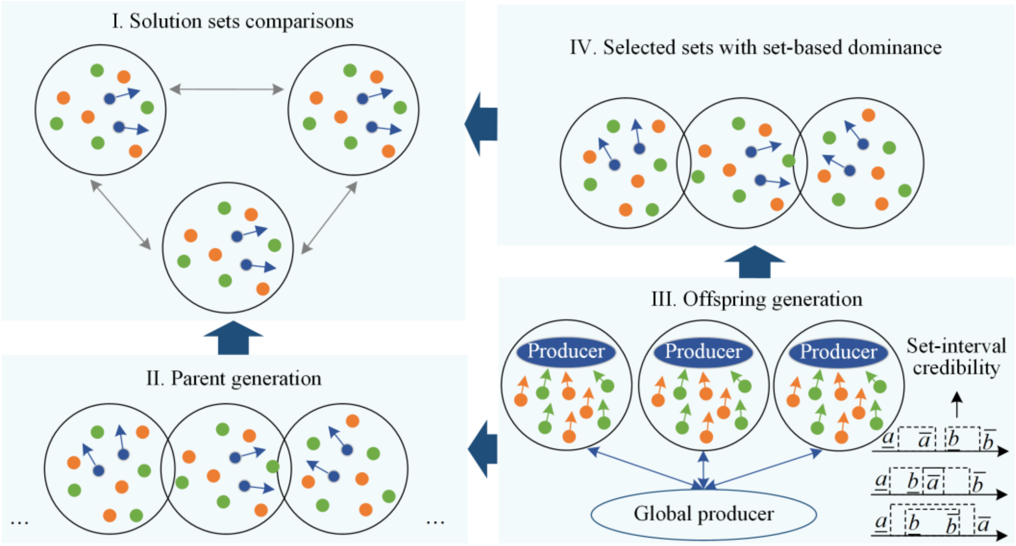

Fig. 3. The evolutionary strategy of Set-GSIO.

Algorithm 1 Set-GSIO Algorithm

```
Input: population size $S$, maximum iterations $T_{\max}$, current iteration $t$, and problem dimension
Output: optimal set-based individuals/Pareto archive $A$
Initialize: Population $S$ ($P$ individuals), set-based bi-objective problem transformation: calculate initial set metrics ($H(X_P)$, $I_{\text{ave}}(X_P)$), initialize Archive $A=\varnothing, t=0$.
while $t < T_{\max}$ do
    Obtain the Pareto solution of each set-based individual from $S$
    Select Parent Set $S_{\text{set}}$ from $S$ for generation
    Select global producer and local producer based on set-interval credibility
    Generate Offspring $S_{\text{offspring}}$ using Set-GSIO roles (scroungers and rangers)
    Combine $S_{\text{new}} = S \cup S_{\text{offspring}}$
    Evaluate $H(X_P)$, $I_{\text{ave}}(X_P)$ or $S_{\text{Spread}}$ metrics for all individuals in $S_{\text{new}}$
    Determine the $S_{\text{new}}$ sets dominance relation and select top $m$ set-based individuals
    Select next generation $S$ and update Archive $A$
    $t \leftarrow t+1$.
end while
```

D. Decision-making Methods

In the decision-making phase, a combination of the Shannon entropy and TOPSIS method is utilized to identify the optimal solution from the Pareto solution set. However, when attempting to identify the optimal and ideal solutions, it is assumed that each attribute is equally weighted. To address this limitation and calculate attribute weights, the Shannon entropy method is employed as described in (36)–(39), elucidating the relative strength of importance by considering the distinctions between data. The complete process of the TOPSIS is outlined in (40)–(42). Moreover, in light of the fact that the interval-based Pareto front is constituted by a series of rectangles, the decision-making process entails the consideration of trade-offs between the midpoint and widths of the interval, with the objective of fully leveraging the potential information inherent in uncertainty. During the Shannon entropy combined with TOPSIS decision-making methods, the data r_{qn} is normalized in advance to facilitate calculations first:

$$r_{qn} = \frac{1/a_{qn}}{\sum_{q=1}^{Q}(1/a_{qn})},\quad q=1,2,\cdots,Q \tag{36}$$

where a_{qn} represent the value of the qth objective for the nth solution. The standard formula for calculating the entropy value e_n of midpoints and widths according to information theory is:

$$e_n = -(\ln q)^{-1}\sum_{q=1}^{Q} r_{qn}\ln r_{qn},\quad n=1,2,\cdots,N \tag{37}$$

The objective weight w_n of the nth criteria with the midpoint w_n^{midpoint} and radius w_n^{radius} is computed as follows:

$$w_n = \frac{1-e_n}{N-\sum_{j=1}^{N} e_n},\quad n=1,\ 2,\ \cdots,\ N \tag{38}$$

Data preprocessing involves constructing a decision matrix z_{qn} with n evaluation criteria and q alternative solutions, followed by the normalization:

$$z_{qn} = \frac{a_{qn}}{\sqrt{\sum_{q=1}^{Q}(a_{qn})^2}},\quad q=1,2,\cdots,Q \tag{39}$$

Then, a weighted matrix is construct based on the weights obtained from the entropy method, and the positive ideal solution and negative ideal solution are determined.

$$\boldsymbol{z}_{qn}^{*} = \boldsymbol{z}_{qn} w_n \tag{40}$$

Finally, the Euclidean distance of each solution from the positive ideal solution and the negative ideal solution is calculated, which is determined by the weighting factor ρ_z of the center ρ_1 and width ρ_2. Once this has been done, calculate score C_q and rank of each alternative to select the final solution.

$$D_q^{\pm} = \sqrt{\sum_{z=1}^{2} \rho_z \sum_{n=1}^{N} \left(\boldsymbol{z}_{qn}^{*} - \boldsymbol{z}_{n}^{*\pm} \right)^2} \tag{41}$$

$$C_q = \frac{D_q^-}{D_q^- + D_q^+} \tag{42}$$

V. Case Study

A. System Description and Configurations

To demonstrate the effectiveness of the proposed optimization framework, the tested IES consists of a modified IEEE 30-bus system, integrated with an IEEE15-node gas network and an IEEE32-node heating network [32], [33]. The system includes various units such as WT, PV, HFC, CHP, P2G, and energy storage devices. The details of the coupling components and their connected nodes within the tested IES network are summarized in Table AI and AII in Appendix A. The details of the topology of the referenced IEEE15-node gas network and IEEE32-node heating network are listed in Tables AIII and AIV in Appendix A, respectively. The IES operates over a 24-hour period with hourly time intervals to capture the dynamic characteristics of energy supply and demand. Numerical simulations are conducted using MATLAB R2021a on a PC equipped with an Intel(R) Core$^{\text{TM}}$ i7-12700H 2.30 GHz CPU and 16 GB of RAM.

The uncertainty in RES output is modeled using a deterministic interval centered around the point forecast. In this study, the uncertainty range is defined by applying a fixed output deviation to the expected output. The RES forecasting method uses a common approach presented in [34] for representing forecasting error bounds. The corresponding uncertainty intervals are illustrated in Fig. A1 in Appendix A. The relevant operating parameters of the energy components and simulation assumptions are listed in Table AV in Appendix A [10], [35]. The parameter settings of the Set-GSIO are determined by an ex-ante performance test using a population size of 330 solutions within a set-based individual (110 individuals in each set), and 120 iterations.

B. Interval Optimization Results and Analysis

1) Performance of the Set-GSIO and Comparison

To determine the final operational solution for the tested IES, a comprehensive evaluation based on the proposed interval multi-objective optimization and decision-making framework is conducted. Acknowledging the uncertainty of RES production, its generation is represented in the form of intervals. As an illustrative example, the multi-objective optimization process generates the interval-based Pareto fronts at some specific moments, as shown in Fig. 4. The interval-based Pareto front is composed of a series of rectangles, with the horizontal and vertical axes representing the system's TFC and CE, respectively. For each rectangle, the length indicates the fluctuation in TFC, while the width represents the potential range of variation in CE.

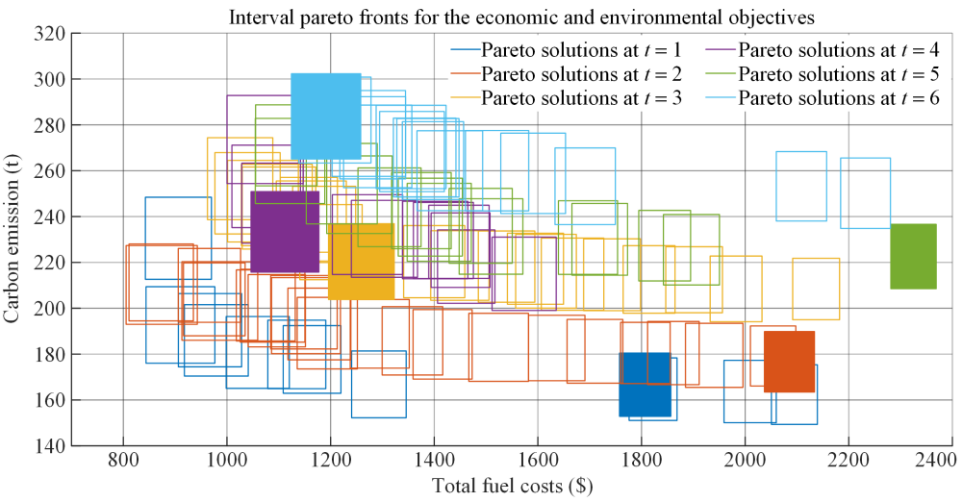

Fig. 4. Derived interval Pareto fronts at some specific moments.

As shown in Fig. 4, the economic and environmental objectives exhibit a trade-off, and the objective functions cannot reach their minimum values simultaneously. In practice, if more favorable environmental outcomes are desired, an increase in the purchase of natural gas with a smaller carbon emission factor but a higher cost per unit for the production of electricity is required, rather than using conventional thermal units. This would result in higher total fuel costs and vice versa. Moreover, the convergence and imprecision of the objectives are also in conflict. Therefore, in the decision-making process, it is essential to consider not only the relative importance of the various objectives but also the relative importance of the convergence and imprecision of the solutions. The color-filled rectangles in Fig. 4 represent the final solution, derived from the decision-making process at each time step, as detailed in the following paragraphs.

To evaluate the performance of the proposed Set-GSIO algorithm, a comparative analysis is conducted against the interval multi-objective optimization evolutionary algorithm based on decomposition (IMOEA/D). In actual implementation, MOEA/D is one of the most efficacious methods for solving multi-objective optimization problems. IMOEA/D is an adaptation of the well-established MOEA/D framework [36] for interval optimization problems and has been validated in similar domains recently [26], [37]. The Pareto front generated by interval multi-objective optimization provides decision makers with a set of solution options, which critically influences the quality of the final solution. Therefore, convergence and diversity of the generated interval Pareto fronts are used as critical indicators for comparing the performance and quality of the solutions. Both algorithms are applied to the aforementioned IES test system under the same computational budget. Given the similarity of the interval multi-objective optimization process at different times, the presented metrics are calculated using the Pareto front statistical data at a specific time. The statistical properties of the resulting Pareto fronts are summarized in Table II.

TABLE II
PERFORMANCE COMPARISON BETWEEN SET-GSIO AND IMOEA/D

Objective	Metric (for interval midpoint)	Algorithm	
		Set-GSIO	IMOEA/D
TFC (\$)	Minimum	**944.2**	1084.6
	Maximum	**2151.2**	2253.5
	Mean	**1429.3**	1618.3
CE (t)	Minimum	**211.6**	239.6
	Maximum	**248.5**	258.2
	Mean	**227.9**	246.3
Performance	$S_{\text{Spread}}(X)$	**1328.5**	1157.7
	$H(X)$	$\mathbf{5.58\times10^4}$	5.12×10^4
	Number of solutions	**23**	20

The results of the metric comparisons demonstrate the superior performance of the proposed Set-GSIO over IMOEA/D. Set-GSIO achieves lower minimum, maximum, and mean values for both the TFC and CE objectives, demonstrating superior convergence.

Specifically, the midpoint mean values of the Pareto front obtained by Set-GSIO achieve reductions of 11.6% and 7.4% in the TFC and CE objectives, respectively, compared to those obtained by IMOEA/D. Furthermore, the superior diversity and spread of the obtained Pareto front are evidenced by the larger $S_{\text{Spread}}(\boldsymbol{X}_{\text{P}})$ metric. The higher HV and greater number of non-dominated solutions confirm Set-GSIO's overall superiority in identifying higher-quality trade-off solutions for the final decision-making.

2) Scalability of the Set-GSIO Algorithm

To validate the scalability of the proposed algorithm for larger systems, this study tests a larger-scale system comprising a modified IEEE118-bus system, integrated with a 20-node gas network and an IEEE32-node heating network. This integration tests the complexity of the simulation and the applicability of the proposed algorithm to larger-scale problems. Due to the complexity of this power system, the modified PCH structure is excluded from the analysis. The IEEE118-bus system comprises 91 load buses and 21 generation buses.

The quality of the final solution is crucially determined by the convergence of the interval Pareto front obtained during the optimization phase. Thus, to further investigate the algorithm's performance on the large-scale case, a parametric study is conducted on the extended large-scale IES case. Figure 5 shows the heatmap of the best Pareto front convergence when varying the population size and the number of iterations for the Set-GSIO. The midpoint values of the interval Pareto solution for the TFC and CE objectives are recorded for each parameter combination. Darker squares represent better convergence of the objective function converges to a lower value. As shown in Fig. 5, both objective functions exhibit roughly consistent trends. By increasing the population size or the number of iterations, the Set-GSIO discovers solutions with better performance. When the population size and the number of iterations reach 400 and 250, respectively, the optimal convergence values of both objectives remain unchanged. This indicates that Set-GSIO can be applied to larger-scale and more complex problems by adjusting the key parameters, and can complete the solution while ensuring a controllable growth of computational resources.

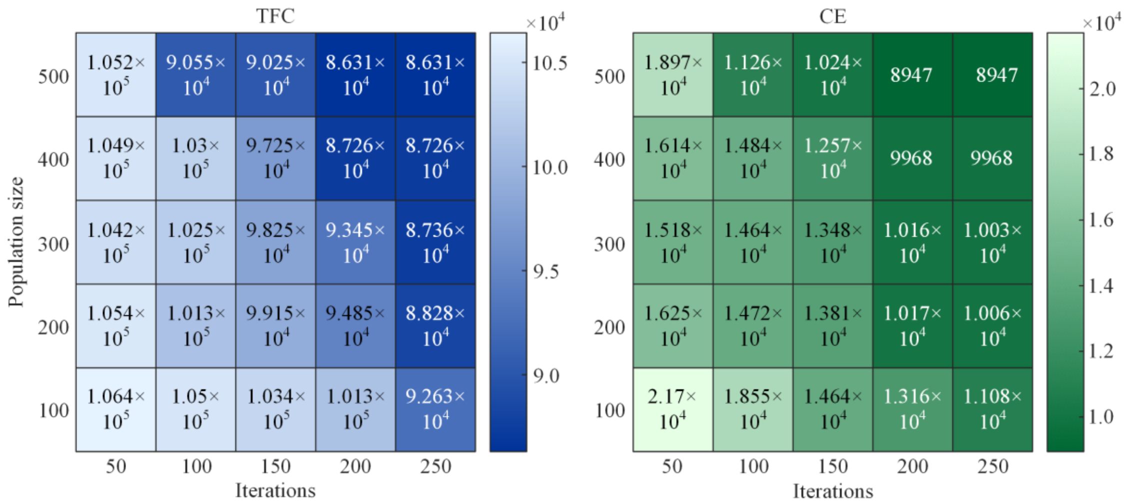

Fig. 5. Heatmap analysis of the optimal objective values with parameters.

3) Decision-making Process

Since the objective function values are represented as interval values, they can be expressed using the interval midpoint $f_q^{\mathrm{M}}(\boldsymbol{x}_{\mathrm{d}},\boldsymbol{u}_{\mathrm{d}})$ and radius $f_q^{\mathrm{R}}(\boldsymbol{x}_{\mathrm{d}},\boldsymbol{u}_{\mathrm{d}})$, as demonstrated in (42). To provide a specific illustration, the moment at time $t = 2$ is used as an example, given the similarity of the decision-making process at different times. In the initial stage, the entropy method is employed to obtain objective weights for the interval midpoint and width of each objective. Subsequently, a weighted sum is performed on the midpoint and width of each objective, as shown in (43). Therefore, the decision problem transforms into one of considering of the convergence and inaccuracy of solutions.

$$\left[f^{\mathrm{M}}(\boldsymbol{x}_{\mathrm{d}},\boldsymbol{u}_{\mathrm{d}}),f^{\mathrm{R}}(\boldsymbol{x}_{\mathrm{d}},\boldsymbol{u}_{\mathrm{d}})\right]=\left[\frac{\underline{f}(\boldsymbol{x}_{\mathrm{d}},\boldsymbol{u}_{\mathrm{d}})+\overline{f}(\boldsymbol{x}_{\mathrm{d}},\boldsymbol{u}_{\mathrm{d}})}{2},\frac{\overline{f}(\boldsymbol{x}_{\mathrm{d}},\boldsymbol{u}_{\mathrm{d}})-\underline{f}(\boldsymbol{x}_{\mathrm{d}},\boldsymbol{u}_{\mathrm{d}})}{2}\right] \tag{42}$$

$$F=\rho_1\left(\sum_{q=1}^{Q}f_q^{\mathrm{M}}(\boldsymbol{x}_{\mathrm{d}},\boldsymbol{u}_{\mathrm{d}})w_j^{\text{midpoint}}\right)+\rho_2\left(\sum_{q=1}^{Q}f_q^{\mathrm{R}}(\boldsymbol{x}_{\mathrm{d}},\boldsymbol{u}_{\mathrm{d}})w_n^{\text{radius}}\right) \tag{43}$$

Table III indicates substantial variations in the midpoint concerning the TFC objective, while the interval width is more influenced by the SVD objective. To comprehensively consider the stability and convergence of solutions, the weights for the midpoint and interval width are both set to 0.5.

TABLE III
THE WEIGHTING COEFFICIENTS AMONG THE OBJECTIVES

	TFC	CE	PL	SVD	SPD
Midpoint	0.8032	0.0376	0.155	0.038	0.0005
Radius	0.0128	0.006	0.0857	0.8954	0.0002

Finally, the TOPSIS method is employed to assess all solutions on the Pareto front. By comparing the rankings derived from these evaluation values, the sixteenth solution is selected as the optimal operating point at time $t = 2$. The aforementioned operating point can be applied to determine the optimization results for electrical, thermal and gas related energy equipment for power generation.

4) Sensitivity to the Forecast Error

As interval optimization is employed to address uncertainty, the accuracy of the renewable source generation forecast interval is of paramount importance regarding the quality of the solution. To investigate the sensitivity of forecast error on the performance of the proposed optimization model, Figs. 6(a) and (b) illustrate the variation of the interval ranges for total fuel costs and carbon emissions, respectively, with respect to different forecast errors and time periods.

As shown in Fig. 7, the interval ranges for both total fuel costs and carbon emissions increase as the forecast error magnitude increases from ±0% to ±50%. This suggests that an elevated forecast error results in amplified uncertainty in the system's operational performance. It is noteworthy that the fluctuations in total fuel costs and carbon emissions are less significant during the time periods from 0–8 hours and 18–24 hours, in comparison to those from 8–18 hours. This is potentially attributable to the fact that during the daytime (8–18 hours), the output of the PV unit exhibits a greater fluctuation range and a higher base output level due to the higher level of solar irradiance. As a result, the uncertainty intervals for RES outputs are higher during the day, contributing to greater fluctuations in the predictions of the two objective functions.

To provide a more intuitive illustration of this trend, a cross-sectional view with the objectives and forecast error at time $t = 2$ is presented in Fig. 7. It is evident that both the mean values and the interval widths of the objectives increase with larger forecast errors. These results suggest that forecast accuracy has a significant influence on the reliability and efficiency of the proposed multi-objective interval optimization. It is thus imperative for operators to ascertain the upper and lower limits of interval-valued uncertain variables with precision through the deployment of meticulous interval forecasting techniques.

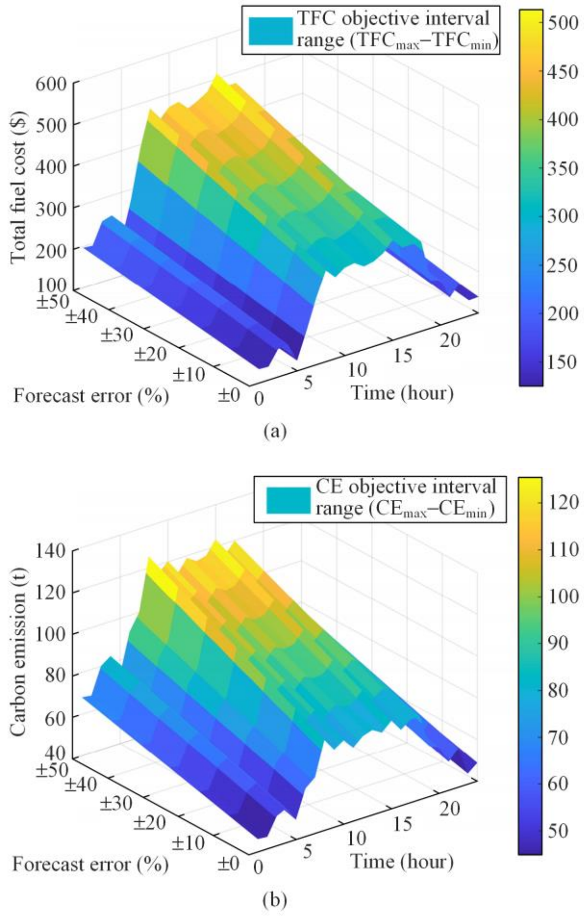

(a)

(b)

Fig. 6. Variation of the objective interval range with forecast error and time. (a) Total fuel cost. (b) Carbon emission.

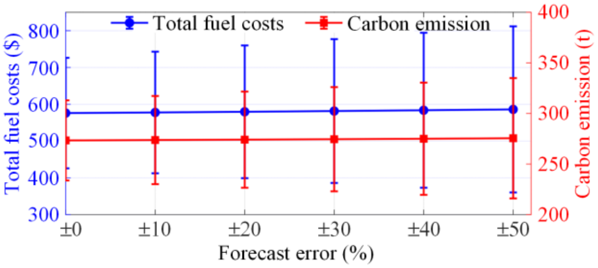

Fig. 7. Sensitivity of renewable output forecast error at time $t = 2$.

C. Comparison with Existing Decision-making Methods

To illustrate the advantages of the proposed decision-making framework, the results are compared with a deterministic transformation approach, which has been adopted in previous work [38]. All other parameter settings remain the same as in the above study.

Case 1: Only the midpoint of interval-value objective functions is considered, as illustrated in (44). This case is consistent with the methodology employed in the study of [38].

$$\min\left[f_1^M(x,u), f_2^M(x,u)\right],\ u\in\left[u^{\mathrm{L}},u^{\mathrm{R}}\right] \tag{44}$$

where u^{L} and u^{R} are the lower and upper bounds of RES outputs, respectively.

Case 2: The midpoint and radius deviations of the interval-valued objective function are co-optimized by a weighting-based approach, as illustrated in (43). This case demonstrates the decision-making framework proposed in this paper.

To compare the performance of the proposed method with existing approaches, a sampling analysis is conducted. Specifically, 500 random samples of power outputs for WT and PV units are generated to represent potential outcomes of the uncertain RES outputs. The solutions obtained from different decision-making methods (Case 1 and Case 2) are then fixed and applied to the aforementioned generated operating scenarios. The performance of these solutions is evaluated in the context of uncertainty under each scenario, and the corresponding results of TFC and CE values are shown in Fig. 8 and Table IV.

As shown in Fig. 8, it is observed that although the decision based solely on optimizing the interval midpoint (Case 1) may yield lower TFC and CE under certain conditions, such decisions may not be effective or truly optimal in practice due to insufficient utilization of the underlying uncertain information. Moreover, the fluctuations in the objective functions for Case 1 are more pronounced, indicating that decision schemes that consider only the interval midpoint are less risk-averse in uncertain environments. When uncertain parameters deviate from their predicted values, the solutions obtained may fail to maintain optimal performance.

In contrast, the co-optimization of the midpoint and radius deviations of the interval-valued objective functions (Case 2) demonstrates more stable performance and robustness under uncertainty when facing with randomly generated scenarios.

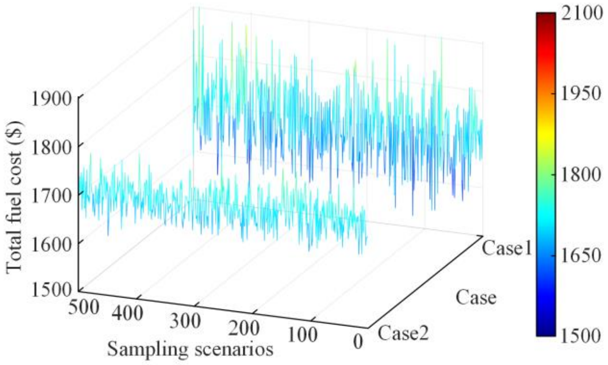

(a)

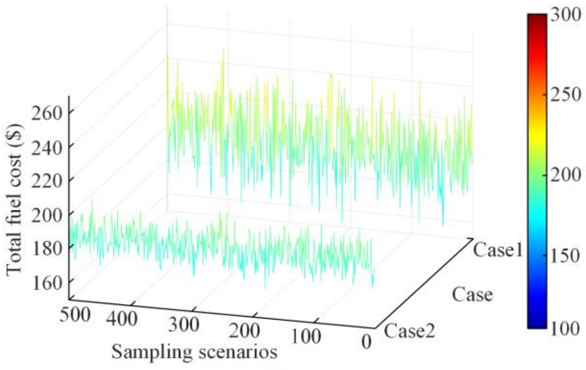

(b)

Fig. 8. Comparison of system operation performances under sampling scenarios at time $t = 2$. (a) Total fuel cost. (b) Carbon emission.

TABLE IV
COMPARISON OF PERFORMANCES WITH DIFFERENT SOLUTION METHODS

Case	Expected performances		Actual performances (500 samples)			
			Average value		Standard deviation	
	TFC	CE	TFC	CE	TFC	CE
1	1661.01	176.81	1779.09	208.45	76.95	18.7
2	1539.98	176.54	1616.23	185.51	31.39	7.84

A detailed examination of the data presented in Table IV reveals that the TFC and CE, when applied to the 500 randomly generated scenarios, represent increases of approximately 7.1% and 17.9%, respectively, in comparison to the expected values in Case 1. However, it is observed that Case 2 can obtain a considerably closer alignment between the expected and actual performances, corresponding to smaller increases of approximately 5.0% in TFC and 5.1% in CE, respectively. Furthermore, the standard deviations in Case 2 are markedly lower, at $31.39 for TFC and 7.84 t for CE, indicating that the system's performance is more consistent and less affected by uncertainties when applying the proposed decision-making framework.

D. Effect of the Incorporation of Hydrogen Storage

To conduct a comparative analysis of the incorporation of hydrogen storage and the utility of the proposed low-carbon economic optimization scheduling model for the tested IES, two scenarios are designed for comparison in this section as follows.

Scenario 1: No consideration of hydrogen storage, refinement of the two-stage operation process in the P2G, and inclusion of the CCS technology.

Scenario 2: Consideration of hydrogen storage, further refinement of the hydrogen flow process in the P2G, and inclusion of the CCS technology.

The comprehensive optimization results for the total of each metric over a 24-hour period are presented in Table V.

TABLE V
OPTIMIZATION RESULTS FOR EACH METRIC FOR DIFFERENT SCENARIOS

	Scenario 1				**Scenario 2**			
	Expected	Maximum	Minimum	Range	Expected	Maximum	Minimum	Range
TFC	**39 095**	40 577	37 614	2963	40 627	42 084	39 170	**2914**
CE	5320	5707	4933	774	**5227**	5618	4850	**768**
PL	273	292.3	254.5	37.8	**266**	283.8	248.4	**35.4**
SVD	8.7315	8.7843	8.6787	0.106	**8.724**	8.7694	8.6787	**0.091**
SPD	5.3538	5.368	5.3397	0.028	**5.3464**	5.3606	5.3322	**0.028**
REC	0.167	0.193	0.138	0.055	**0.072**	0.092	0.051	**0.041**

As shown in Table V, the incorporation of hydrogen energy storage facilitates the absorption of CO_2 for synthesis gas synthesis by MR within the PCH structure. This process allows surplus RES to be converted into hydrogen, which is subsequently transformed back into electricity and thermal energy during periods of peak demand. Moreover, it also reduces the power requirements of various devices, thereby minimizing the overall carbon emissions of the system. Specifically, the expected CE in Scenario 2 decreased by approximately 1.62% compared to Scenario 1, dropping from 5320 to 5234 t. However, despite the slight increase in TFC in Scenario 2, the stability of the solutions in Scenario 2 is superior, as evidenced by the smaller interval radius between the maximum and minimum values of the performance metrics. For instance, the interval range for CE in Scenario 2 is 768 t (from 4850 t to 5618 t), which is narrower than the 774 t range in Scenario 1. This indicates enhanced predictability and reliability of system performance. Thus, it can be seen that while integrating hydrogen energy storage enhances environmental performance and solution stability, it also introduces a conflict with cost minimization. In addition, there is an inherent conflict between TFC and CE objectives, as evidenced by the expected TFC in Scenario 2 being lower than that in Scenario 1 and the trend shown in the interval Pareto front in Fig. 4. Furthermore, the energy conversion cycle associated with hydrogen storage is subject to round-trip efficiency losses. To compensate for these energy losses while still meeting system demand, a marginal increase in natural gas consumption from other units may be required, thus contributing to the higher TFC.

1) Hydrogen Flow

Figure 9 depicts the operational dynamics of two scenarios in terms of hydrogen energy flow, where Figs. 9(a), (b), and (c) respectively showcase the hydrogen power profiles of the MR, HFC, and EL in two scenarios, ensuring compliance with the hydrogen energy balance constraints among the components.

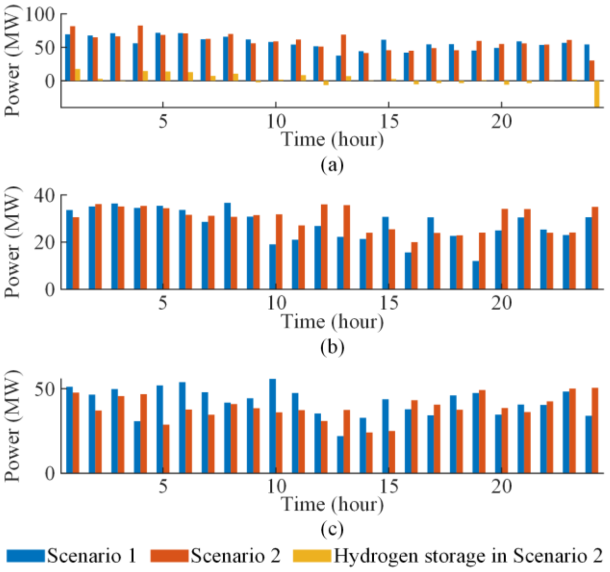

Fig. 9. Operation results of IES from the perspective of hydrogen flow. (a) Hydrogen flow of EL. (b) Hydrogen flow of HFC. (c) Hydrogen flow of MR.

The preceding results illustrate the overall operational trends of the hydrogen energy flow. It is noteworthy that the hydrogen production of the EL exhibits significant variations between Scenario 1 and Scenario 2 between 11:00 and 19:00. This discrepancy can be attributed to the surplus RES, particularly the increased PV generation during these periods. The surplus electricity is then converted into stored hydrogen or synthesized into SNG. Moreover, during the periods of high wind power output, the EL with hydrogen storage employs a strategy of storing excess electricity as hydrogen. The approach results in a reduction in the power consumption of the EL during other time frames in comparison to the system without hydrogen storage. As illustrated in Figs. 9(b) and (c), in the final moment, the hydrogen consumption of both the HFC and MR is almost at its highest level of the entire period, resulting in a larger negative output for the hydrogen storage in Scenario 2, as shown in Fig. 9(a). Finally, the MR exhibits the highest hydrogen consumption, likely due to its association with the CE target. The increased hydrogen power in MR results in more substantial carbon capture by the CCS, consequently leading to a reduction in carbon emissions.

2) Power Flow Analysis of the Modified PCH Structure

Figure 10 depicts the electrical power input, thermal power output, and the production of SNG across the entire PCH structure. Figure 10(a) shows that while incorporating hydrogen storage raises the total electrical power consumption of the PCH structure, this increase is essential, as it necessitates a greater quantity of hydrogen, subsequently boosting the power requirements of the EL. Nevertheless, the peak demand for hydrogen typically coincides with periods of high PV output, facilitating a more efficient utilization of RES. Figure 10(c) reveals that the integration of hydrogen storage enhances the conversion of additional hydrogen and CO_2 into SNG, which in turn leads to a decrease in the system's overall carbon emissions, compared to a scenario without hydrogen storage.

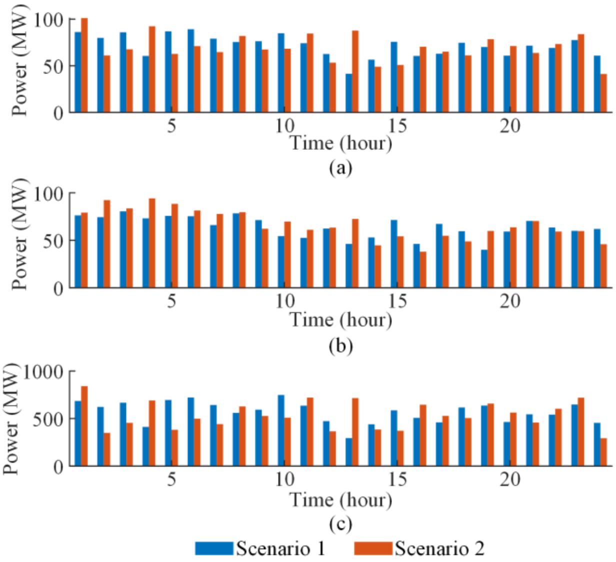

Fig. 10. Operation results of energy input and output of the modified PCH structure. (a) Electrical power. (b) Thermal power. (c) Gas power.

Table VI provides a detailed comparison of carbon emission reductions in Scenario 2 relative to Scenario 1 at each hourly interval. As seen in Table VI, it is evident that during the time frames from 01:00 to 10:00 and 14:00 to 22:00, the IES equipped with hydrogen storage consistently exhibits lower CO_2 emissions compared to the IES without hydrogen storage.

TABLE VI

THE DETAILED OF CARBON EMISSION REDUCTION IN SCENARIO 2 OF EACH MOMENT COMPARED TO SCENARIO 1

Time (hour)	1	2	3	4	5	6	7	8	9	10	11	12
Carbon Emission reduction (t)	–3.75	10.3	12.28	3.52	9.42	12.43	14.86	5.43	11.09	19.26	–5.15	3.69
Time (hour)	13	14	15	16	17	18	19	20	21	22	23	24
Carbon Emission reduction (t)	–22.26	7.99	20.63	–2.39	–6.61	14.43	4.97	6.21	8.09	0.25	–3.66	–28.07

This reduction is primarily attributed to the system's ability to convert excess RES into stored hydrogen, which allows the MR process to produce more natural gas while simultaneously enhancing CO_2 absorption capabilities. Simultaneously, the generated natural gas and the stored hydrogen contribute to the energy supply of the IES through GB and HFC, decreasing the reliance on external gas supplies and reducing the output from generators, thereby indirectly lowering the overall carbon emissions of the IES. A detailed examination of Table VI reveals that in 13 out of the 24-hourly intervals, Scenario 2 achieves varying degrees of CO_2 emission reduction, ranging from 5.43 t to 20.63 t. Notably, the maximum reduction occurs at 15:00 with a decrease of 20.63 t, followed by 10:00 at 19.26 t. Such significant reductions are predominantly observed during periods of high RES output, where excess energy is efficiently converted into hydrogen for storage, which subsequently displaces traditional fossil fuel usage, thereby enhancing the system's overall carbon efficiency. Overall, the aggregate data indicates that Scenario 2 successfully reduces total daily CO_2 emissions by 92.95 t, representing a 2.1% decrease compared to Scenario 1.

VI. CONCLUSION AND FUTURE RESEARCH

This paper proposes an interval low-carbon dispatch model that integrates hydrogen storage with P2G, CCS, and HFC as a structure embedded within an IES with electricity, heating, and gas subsystems. A multi-objective interval optimization method, namely Set-GSIO, is developed to construct interval-based Pareto fronts under uncertain renewable generation. The final selection of dispatch solutions is guided by a Shannon entropy-TOPSIS decision-making process, incorporating security metrics to address both the midpoint and radius of the interval objectives.

Case studies on a modified IEEE30-bus system integrated with a 15-node gas network and a 32-node heat network verify the synergy between hydrogen storage and the PCH structure. Compared to the original configuration, the proposed structure enhances flexibility and achieves a 9.5% reduction in renewable energy curtailment and a 2.1% reduction in total daily carbon emissions. Additionally, the proposed Set-GSIO algorithm shows its superiority in convergence and performance compared to IMOEA/D and verifies its scalability on a larger-scale IES network. Results show that interval-based optimization can better manage the variability of RES than deterministic methods, and the proposed decision-making framework maintains essential uncertain information while achieving robust dispatch strategies.

Future work will investigate decentralized optimization frameworks that accommodate multiple independent stakeholders, reflecting real-world IES configurations. Additionally, Set-GSIO will be extended for larger-scale systems with complex topologies by reducing computational burden, potentially through surrogate modeling to approximate costly power flow analysis and further accelerate the optimization process.

APPENDIX A

A. Component-level Constraints

1) Electrical Power Balance

$$\begin{gathered}P_{\mathrm{gen},t}+P_{\mathrm{WT},t}+P_{\mathrm{PV},t}+P_{\mathrm{CHP,e},t}+P_{\mathrm{HFC,e},t}+P_{\mathrm{ES,e},t}=\\ P_{\mathrm{e,load}}+P_{\mathrm{CMP},t}+P_{\mathrm{E}}\end{gathered}\tag{A1}$$

where P_{E} represents the input power at time t for the PCH and hydrogen storage equipment structure; while $P_{\mathrm{ES,e},t}$ and $P_{\mathrm{e,load}}$ represent the output power of the battery energy storage system and electrical load at time t.

2) Thermal Power Balance

$$Q_{\mathrm{HFC,h},t}+Q_{\mathrm{GB,h},t}+Q_{\mathrm{CHP,h},t}=Q_{\mathrm{load,h},t}\tag{A2}$$

where $Q_{\mathrm{load,h},t}$ represents the thermal load at time t.

3) Gas Power Balance

$$P_{\mathrm{g,gas},t}+P_{\mathrm{MR,g},t}=P_{\mathrm{g,load},t}+P_{\mathrm{CHP,g},t}+P_{\mathrm{GB,g},t}\tag{A3}$$

where $P_{\mathrm{g,load},t}$ represents the gas load at time t; and $P_{\mathrm{g,gas},t}$ is the natural gas emitted by the gas source.

4) The Constraints of CHP

$$\begin{cases}0\leqslant P_{\mathrm{CHP,e},t}\leqslant P_{\mathrm{CHP,e},t}^{\max}\\ 0\leqslant Q_{\mathrm{CHP,h},t}\leqslant Q_{\mathrm{CHP,h},t}^{\max}\end{cases}\tag{A4}$$

where $P_{\mathrm{CHP,e},t}^{\max}$ and $Q_{\mathrm{CHP,h},t}^{\max}$ are the upper limits of the electrical and thermal power output of the CHP unit at time t, respectively.

5) The Constraints of HFC

$$\begin{cases}0\leqslant P_{\mathrm{HFC,e},t}\leqslant P_{\mathrm{HFC,e},t}^{\max}\\ 0\leqslant Q_{\mathrm{HFC,h},t}\leqslant Q_{\mathrm{HFC,h},t}^{\max}\end{cases}\tag{A5}$$

where $P_{\mathrm{HFC,e},t}^{\max}$ and $Q_{\mathrm{HFC,h},t}^{\max}$ are the upper limits of the electrical and thermal power output of the HFC unit at time t, respectively.

6) Storage Equipment Constraints

The energy storage devices considered in this paper include electricity and hydrogen storage, which can be expressed by a general formula [12]:

$$\begin{cases}0\leqslant P_{\mathrm{es},n,t}^{\mathrm{cha}}\leqslant B_{\mathrm{es},n,t}^{\mathrm{cha}}P_{\mathrm{es},n,\max}\\ 0\leqslant P_{\mathrm{es},n,t}^{\mathrm{dis}}\leqslant B_{\mathrm{es},n,t}^{\mathrm{dis}}P_{\mathrm{es},n,\max}\\ P_{\mathrm{es},n,t}=P_{\mathrm{es},n,t}^{\mathrm{cha}}\eta_{\mathrm{es},n}^{\mathrm{cha}}-P_{\mathrm{es},n,t}^{\mathrm{dis}}\eta_{\mathrm{es},n}^{\mathrm{dis}}\\ S_n(t)=S_n(t-1)+P_{\mathrm{es},n,\mathrm{t}}\big/P_{\mathrm{es},n}^{\mathrm{cap}}\\ S_n(1)=S_n(T)\\ B_{\mathrm{es},n,t}^{\mathrm{cha}}+B_{\mathrm{es},n,t}^{\mathrm{dis}}=1\quad\text{(Battery-operated only)}\\ S_{n,\min}\leqslant S_n(t)\leqslant S_{n,\max}\end{cases}\tag{A6}$$

where $P_{\mathrm{es},n,t}^{\mathrm{cha}}$ and $P_{\mathrm{es},n,t}^{\mathrm{dis}}$ represent the power for charging and discharging of the *n*th energy storage device during the time *t*; $P_{\mathrm{es},n,\max}$ is the maximum power for both charging and discharging operations of the *n*th energy storage device; while $B_{\mathrm{es},n,t}^{\mathrm{cha}}$ and $B_{\mathrm{es},n,t}^{\mathrm{dis}}$ are binary variables, $B_{\mathrm{es},n,t}^{\mathrm{cha}}=1$ and $B_{\mathrm{es},n,t}^{\mathrm{dis}}=0$ indicate that it is charging, while $B_{\mathrm{es},n,t}^{\mathrm{cha}}=0$ and $B_{\mathrm{es},n,t}^{\mathrm{dis}}=1$ suggest it is discharging; $P_{\mathrm{es},n,t}$ signifies the ultimate power output of the *n*th energy storage device at time *t*; $\eta_{\mathrm{es},n}^{\mathrm{cha}}$ and $\eta_{\mathrm{es},n}^{\mathrm{dis}}$ denote efficiency during the charging and discharging processes of the *n*th energy storage device; $S_n(t)$ represents the capacity of the *n*th energy storage device at time *t*; $P_{\mathrm{es},n}^{\mathrm{cap}}$ denotes the rated capacity of the *n*th energy storage device; while $S_{n,\min}$ and $S_{n,\max}$ define the minimum and maximum capacity limits of the *n*th energy storage device, respectively.

B. Tested IES Network Connection

TABLE AI

MODIFIED IEEE30-BUS SYSTEM, INTEGRATED WITH AN IEEE15-NODE GAS NETWORK, AND AN IEEE32-NODE HEATING NETWORK

Network	Component	Node
Electricity (IEEE30-bus [33])	CHP	8, 13, 23, 25, 27
	PCH (in connection with CCS and EL)	9, 22
	Battery energy storage	18, 25
	WT	5, 8, 25
	PV	6, 9, 22
Heating (IEEE32-node [30])	CHP	1, 31, 32
	PCH (in connection with HFC)	11, 29
	GB	4, 11
Gas (IEEE15-node [32])	CHP	3, 4, 13, 14, 15
	PCH (in connection with MR)	1, 2
	GB	3, 13

TABLE AII

MODIFIED IEEE118-BUS SYSTEM, INTEGRATED WITH A 20-NODE GAS NETWORK, AND AN IEEE32-NODE HEATING NETWORK

Network	Component	Node
Electricity (IEEE118-bus [33])	WT	59, 61, 100, 111
	PV	12, 46, 54, 103
	CHP	25, 36, 40, 49
	P2G	7, 23, 113
Gas (20-node [30])	CHP	3, 12, 15, 20
	P2G	2, 5, 14
Heating (IEEE32-node [32])	CHP	1

C. Details of the Tested Integrated Energy Systems

TABLE AIII

DETAILS OF THE REFERENCED 15-NODE NATURAL GAS NETWORK

Node	Type	Load (SCF/hr)	Supply (SCF/hr)	Pressure (kPa)	Min pressure (kPa)	Max pressure (kPa)
1	1	0	7.288×10^6	1000	600	1200
2	1	0	6.867×10^6	978.63	600	1200
3	2	3.838×10^6	0	729.716	500	1200
4	2	1.218×10^6	0	737.345	500	1200
5	3	0	0	575.481	400	1200
6	4	0	0	1035	400	1200
7	3	0	0	607.588	400	1200
8	4	0	0	1154.4	400	1200
9	3	0	0	918.628	400	1200
10	4	0	0	951	400	1200
11	3	0	0	932.81	400	1200
12	4	0	0	932.82	400	1200
13	2	4.263×10^6	0	601.554	600	1000
14	2	4.274×10^6	0	600.778	600	1000
15	2	0.501×10^6	0	600	600	1000

Note: node type 1—reference node; node type type 2—load node; node type 3—compressor inlet node; node type 4—compressor outlet node.

TABLE AIV

DETAILS OF THE REFERENCED 32-NODE HEAT NETWORK

Node	Type	Load (kJ)	$T_\mathrm{s}^{\min}$ (°C)	$T_\mathrm{s}^{\max}$ (°C)	$T_\mathrm{r}^{\min}$ (°C)	$T_\mathrm{r}^{\max}$ (°C)
1	1	0	110	120	60	80
2	2	0	110	120	60	80
3	2	10.7	110	120	60	80
4	2	14.5	110	120	60	80
5	2	0	110	120	60	80
6	2	10.7	110	120	60	80
7	2	10.7	110	120	60	80
8	2	10.7	110	120	60	80
9	2	10.7	110	120	60	80
10	2	10.7	110	120	60	80
11	2	25	110	120	60	80
12	2	10.7	110	120	60	80
13	2	0	110	120	60	80
14	2	10.7	110	120	60	80
15	2	0	110	120	60	80
16	2	8.5	110	120	60	80
17	2	8.5	110	120	60	80
18	2	8.5	110	120	60	80
19	2	0	110	120	60	80
20	2	8.5	110	120	60	80
21	2	8.5	110	120	60	80
22	2	0	110	120	60	80
23	2	10.7	110	120	60	80
24	2	10.7	110	120	60	80
25	2	0	110	120	60	80
26	2	10.7	110	120	60	80
27	2	10.7	110	120	60	80
28	2	0	110	120	60	80
29	2	20.7	110	120	60	80
30	2	10.7	110	120	60	80
31	3	−10	110	120	60	80
32	3	−100	110	120	60	80

Note: $T_\mathrm{s}^{\min}$ and $T_\mathrm{s}^{\max}$ are minimum and maximum supply temperatures in degrees Celsius (°C); $T_\mathrm{r}^{\min}$ and $T_\mathrm{r}^{\max}$ are minimum and maximum return temperatures in degrees Celsius (°C); node type 1—reference node; node type 2—load node; node type 3—source node.

D. Technical and Economic Parameters

TABLE AV
THE RELEVANT OPERATING PARAMETERS OF THE DEVICES

Technical parameter	Variable	Values	Reference
Energy conversion efficiency of EL	$T_{\mathrm{s}}^{\min}$	0.7	[10]
Energy conversion efficiency of MR	η_{MR}	0.6	[10]
Thermal conversion efficiency of HFC	$\eta_{\mathrm{HFC,h}}$	0.35	[10]
Electrical conversion efficiency of HFC	$\eta_{\mathrm{HFC,e}}$	0.5	[10]
Power conversion coefficient of compressor	η_{CMP}	0.78	[30]
Thermal conversion efficiency of GB	$\eta_{\mathrm{GB,h}}$	0.95	[10]
Carbon emission calculation parameters of coal-fired units	α_1	36	[35]
	β_1	−0.38	[35]
	γ_1	0.0034	[35]
Carbon emission calculation parameters of gas-consumed energy supply device	α_2	3	[35]
	β_2	−0.004	[35]
	γ_2	0.001	[35]
MR carbon-to-gas conversion efficiency	ϖ	1	[10]
Nature gas price ($/kWh)	C_{g}	0.05	[10]
Carbon emission quota factors of electricity consumption (kg/kWh)	χ_{e}	0.728	[10]
Carbon emission quota factors of natural gas consumption (kg/kWh)	χ_{g}	0.234	[10]
Low calorific value of natural gas (kWh/m^3)	$L_{\mathrm{LHV,ng}}$	9.7	[10]

E. Wind and Solar Interval Output

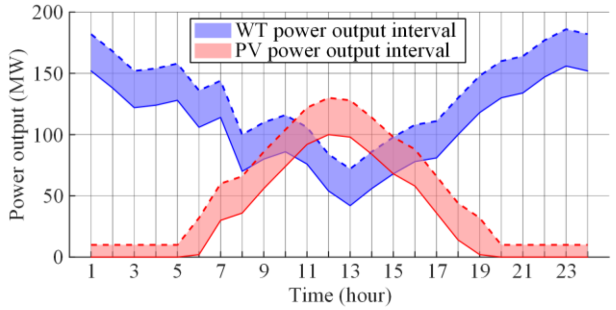

Fig. A1. Wind and solar output forecast data with uncertain interval.

ACKNOWLEDGMENT

The authors would like to acknowledge the support of the Institute of Smart Energy Network and Its Automation, South China University of Technology, Guangzhou, China.

AUTHORS' CONTRIBUTIONS

Jiehui Zheng: methodology, writing review, editing, validation, and conceptualization. Lexian Zhai: writing original draft, software, and visualization. Mingming Tao: writing review, editing, and visualization. Wenhu Tang: supervision and writing review. Zhigang Li: methodology, supervision, and writing review. All authors read and approved the final manuscript.

FUNDING

This work is supported by the National Natural Science Foundation of China (No. 52477097), and the GuangDong Basic and Applied Basic Research Foundation (No. 2024A1515240034).

AVAILABILITY OF DATA AND MATERIALS

Not applicable.

DECLARATIONS

Competing interests: The authors declare that they have no known competing financial interests or personal relationships that could have appeared to influence the work reported in this article.

AUTHORS' INFORMATION

Jiehui Zheng received the B.E. degree from the Huazhong University of Science and Technology, Wuhan, China, in 2012, and the Ph.D degree from the South China University of Technology, Guangzhou, China, in 2017, all in electrical engineering. He is currently an associate professor with the School of Electric Power Engineering, South China University of Technology. His research interests include optimization algorithm, decision-making method, and their application on integrated energy system.

Lexian Zhai received the B.E. degree in electrical engineering from Beijing Jiaotong University, Beijing, China, in 2023. He is currently pursuing the M.S. degree in electrical engineering with the School of Electric Power Engineering, South China University of Technology, Guangzhou, China. His research interests include optimization algorithms, decision-making methods, and their applications in the planning and operation of multi-energy complementary power systems.

Mingming Tao received the B.E. degree in electrical engineering from Nanchang University, Nanchang, China, in 2021, and the M.S. degree in electrical engineering from the School of Electric Power Engineering, South China University of Technology, Guangzhou, China, in 2024. His research interests include optimization algorithms, decision-making methods, and their applications in integrated energy systems.

Wenhu Tang received the B.Eng. and M.Sc. degrees in electrical engineering from Huazhong University of Science and Technology, Wuhan, China, in 1996 and 2000, respectively, and the Ph.D. degree in electrical engineering from The University of Liverpool Liverpool, UK, in 2004. He was a postdoctoral research associate and subsequently a lecturer at The University of Liverpool between 2004 and 2013. He is currently a distinguished professor and dean of the School of Electric Power Engineering, South China University of Technology, Guangzhou, China. He has authored and coauthored more than 150 research papers and 1Springer research monograph. His research interests include renewable energy integration in power grids, condition monitoring and fault diagnosis for power apparatus and power system resilience assessment.

Zhigang Li received the B.E. and Ph.D. degrees from the Department of Electrical Engineering and Applied Electronic Technology of Tsinghua University, Beijing, China, in 2011 and 2016, respectively. He is currently an assistant professor with the Chinese University of Hong Kong, Shenzhen. His research interests include smart grid, integrated energy systems, renewable energy, optimization theory and artificial intelligence.

REFERENCES

[1] P. Xie, S. Lü, and D. Liu *et al*. "Low-carbon economic optimal dispatch of thermal-wind-solar-storage systems considering interval differentiation of thermal power carbon emission intensity,". *Power System Protection and Control*, vol. 53, no. 13, pp. 142-151, Jul. 2025. (in Chinese)

[2] P. Zhang, W. Cai, and M. Yao *et al.*, "Urban carbon emissions associated with electricity consumption in Beijing and the driving factors," *Applied Energy*, vol. 275, Oct. 2020.

[3] D. Xu, Z. Cai, and Q. Cheng *et al.*, "Security-constrained transmission maintenance optimization considering generation and operational risk costs," *Journal of Modern Power Systems and Clean Energy*, vol. 12, no. 3, pp. 767-781, Sept. 2023.

[4] C. Wu, H. Hong, and C. L. Tseng *et al.*, "Economic dispatch of CAES in an integrated energy system with cooling, heating, and electricity supplies," *Energy Conversion and Economics*, vol. 4, no. 1, pp. 61-72, Feb. 2023.

[5] M. Qin, Y. Yang, and X. Zhao *et al.*, "Low-carbon economic multi-objective dispatch of integrated energy system considering the price fluctuation of natural gas and carbon emission accounting," *Protection and Control of Modern Power Systems*, vol. 8, no. 4, pp. 1-18, Dec. 2023.

[6] C. Pan, T. Jin, and N. Li *et al.*, "Multi-objective and two-stage optimization study of integrated energy systems considering P2G and integrated demand responses," *Energy*, vol. 270, May 2023.

[7] Y. Li, Y. Zou, and Y. Tan *et al.*, "Optimal stochastic operation of integrated low-carbon electric power, natural gas, and heat delivery system," *IEEE Transactions on Sustainable Energy*, vol. 9, no. 1, pp. 273-283, Jan. 2017.

[8] Y. Tao, J. Qiu, and S. Lai *et al.*, "Carbon-oriented electricity network planning and transformation," *IEEE Transactions on Power Systems*, vol. 36, no. 2, pp. 1034-1048, Aug. 2020.

[9] Y. Ma, H. Wang, and F. Hong *et al.*, "Modeling and optimization of combined heat and power with power-to-gas and carbon capture system in integrated energy system," *Energy*, vol. 236, Dec. 2021.

[10] J. Wang, J. Mao, and R. Hao *et al.*, "Multi-energy coupling analysis and optimal scheduling of regional integrated energy system," *Energy*, vol. 254, Sept. 2022.

[11] J. Zheng, J. Guo, and Z. Li *et al.*, "Optimal design for a multi-level energy exploitation unit based on hydrogen storage combining methane reactor and carbon capture, utilization and storage," *Journal of Energy Storage*, vol. 62, Jun. 2023.

[12] W. Zhang and C. Xu, "Capacity configuration optimization of photovoltaic-battery-electrolysis hybrid system for hydrogen generation considering dynamic efficiency and cost learning," *Energy Conversion and Economics*, vol. 5, no. 2, pp. 78-92, Apr. 2024.

[13] Y. Wang, C. Liu, and Y. Qin *et al.*, "Synergistic planning of an integrated energy system containing hydrogen storage with the coupled use of electric-thermal energy," *International Journal of Hydrogen Energy*, vol. 48, no. 40, pp. 15154-15178, May 2023.

[14] M. Daraei, P. E. Campana, and E. Thorin, "Power-to-hydrogen storage integrated with rooftop photovoltaic systems and combined heat and power plants," *Applied Energy*, vol. 276, Oct. 2020.

[15] T. Wang, Z. Huang, and R. Ying *et al.*, "A low-carbon operation optimization method of ETG-RIES based on adaptive optimization spiking neural P systems," *Protection and Control of Modern Power Systems*, vol. 9, no. 5, pp. 162-177, Sept. 2024.

[16] J. Zheng, W. Xiao, and C. Wu *et al.*, "A gradient descent direction based-cumulants method for probabilistic energy flow analysis of individual-based integrated energy systems," *Energy*, vol. 265, Feb. 2023.

[17] J. Yu , D. Yang , and J. Cao *et al.*, "Robust state estimation for an electricity-gas-heat integrated energy system considering dynamic characteristics," *Protection and Control of Modern Power Systems*, vol.9, no.1, pp. 65-80, Jan. 2024.

[18] Y. Lei, D. Wang, and H. Cheng *et al.*, "A three-layer planning framework for regional integrated energy systems based on the quasi-quantum theory," *International Journal of Electrical Power & Energy Systems*, vol. 155, Jan. 2024.

[19] T. Ren, R. Li, and X. Li, "Bi-level multi-objective robust optimization for performance improvements in integrated energy system with solar fuel production," *Renewable Energy*, vol. 219, Dec. 2023.

[20] Z. Zhang, C. Wang, and Q. Wu *et al.*, "Optimal dispatch for cross-regional integrated energy system with renewable energy uncertainties: a unified spatial-temporal cooperative framework," *Energy*, vol. 292, Apr. 2024.

[21] X. Yang, X. Wang, and Y. Deng *et al.*, "Integrated energy system scheduling model based on non-complete interval multi-objective fuzzy optimization," *Renewable Energy*, vol. 218, Dec. 2023.

[22] J. Yang and C. Su, "Robust optimization of microgrid based on renewable distributed power generation and

load demand uncertainty," *Energy*, vol. 223, May 2021.

[23] M. Yin, K. Li, and J. Yu, "A data-driven approach for microgrid distributed generation planning under uncertainties," *Applied Energy*, vol. 309, Mar. 2022.

[24] C. Wan, K. Zhang, and C. Zhao *et al.* (2025, Aug.), "An integrated probabilistic forecasting and robust optimization method for AC-OPF under high-penetration renewable energy," *IEEE Transactions on Sustainable Energy*, [Online], pp. 1-15. Available: https://ieeexplore.ieee.org/abstract/document/11112675

[25] Y. Dong, H. Zhang, and P. Ma *et al.*, "A hybrid robust-interval optimization approach for integrated energy systems planning under uncertainties," *Energy*, vol. 274, Jul. 2023.

[26] B. Zeng, W. Zhang, and P. Hu *et al.*, "Synergetic renewable generation allocation and 5G base station placement for decarbonizing development of power distribution system: a multi-objective interval evolutionary optimization approach," *Applied Energy*, vol. 351, Dec. 2023.

[27] X. Sheng, S. Lin, and W. Liang *et al.*, "Interval economic dispatch for commercial campus integrated energy system with demand response considering multiple uncertainties," *CSEE Journal of Power and Energy Systems*, vol. 11, no. 3, pp. 1297-1311, Jul. 2024.

[28] H. T. Nguyen, U. Safder, and X. N. Nguyen *et al.*, "Multi-objective decision-making and optimal sizing of a hybrid renewable energy system to meet the dynamic energy demands of a wastewater treatment plant," *Energy*, vol. 191, Jan. 2020.

[29] Y. Wang, X. Wang, and H. Yu *et al.*, "Optimal design of integrated energy system considering economics, autonomy and carbon emissions," *Journal of Cleaner Production*, vol. 225, pp. 563-578, Jul. 2019.

[30] J. Zheng, Q. Wu, and Z. Jing, "Coordinated scheduling strategy to optimize conflicting benefits for daily operation of integrated electricity and gas networks," *Applied energy*, vol. 192, pp. 370-381, Apr. 2017.

[31] J. Zheng, J. Chen, and Q. Wu *et al.*, "Multi-objective optimization and decision making for power dispatch of a large-scale integrated energy system with distributed DHCS embedded," *Applied Energy*, vol. 154, pp. 369-379, Sept. 2015.

[32] X. Liu, J. Wu, and N. Jenkins *et al.*, "Combined analysis of electricity and heat networks," *Applied Energy*, vol. 162, pp. 1238-1250, Jan. 2016.

[33] R. D. Zimmerman, C. E. Murillo-S´anchez, and R. J. Thomas, "Matpower: steady-state operations, planning, and analysis tools for power systems research and education," *IEEE Transactions on Power Systems*, vol. 26, no. 1, pp. 12-19, Feb. 2010.

[34] C. Wan, Z. Xu, and P. Pinson, "Direct interval forecasting of wind power," *IEEE Transactions on Power Systems*, vol. 28, no. 4, pp. 4877-4878, Nov. 2013.

[35] J. Xu, C. Gao, and Z. Yan *et al.*, "Low carbon optimal operation of integrated energy systems considering air pollution emissions," *Energy Reports*, vol. 9, pp. 1597-1606, Sept. 2023.

[36] Q. Zhang and H. Li, "MOEA/D: a multiobjective evolutionary algorithm based on decomposition," *IEEE Transactions on Evolutionary Computation*, vol. 11, no. 6, pp. 712-731, Dec. 2007.

[37] Y. Zhang, C. Liang, and H. Wang *et al.*, "A multi-objective interval optimization approach to expansion planning of active distribution system with distributed internet data centers and renewable energy resources," *IET Generation, Transmission & Distribution*, vol. 18, no. 18, pp. 2999-3016, Sept. 2024.

[38] Y. Li, P. Wang, and H. B. Gooi *et al.*, "Multi-objective optimal dispatch of microgrid under uncertainties via interval optimization," *IEEE Transactions on Smart Grid*, vol. 10, no. 2, pp. 2046-2058, Dec. 2017.